Universiteit Leiden
The Netherlands

Precision modeling of breast cancer in the CRISPR era

Annunziato, S.

Citation
Annunziato, S. (2020, January 16). *Precision modeling of breast cancer in the CRISPR era*. Retrieved from https://hdl.handle.net/1887/82703

Version:	Publisher's Version
License:	Licence agreement concerning inclusion of doctoral thesis in the Institutional Repository of the University of Leiden
Downloaded from:	https://hdl.handle.net/1887/82703

Note: To cite this publication please use the final published version (if applicable).

Cover Page

Universiteit Leiden

Leiden University Repository

The handle http://hdl.handle.net/1887/82703 holds various files of this Leiden University dissertation.

Author: Annunziato, S.
Title: Precision modeling of breast cancer in the CRISPR era
Issue Date: 2020-01-16

5

Comparative oncogenomics identifies combinations of driver genes and drug targets in *BRCA1*-mutated breast cancer

Stefano Annunziato[a,i,*], Julian R. de Ruiter[a,b,i,*], Linda Henneman[a,c,*], Chiara S. Brambillasca[a,i,*], Catrin Lutz[a,i], François Vaillant[d,e], Federica Ferrante[a,i], Anne Paulien Drenth[a,i], Eline van der Burg[a,i], Bjørn Siteur[f], Bas van Gerwen[f], Roebi de Bruijn[a,b,i], Martine H. van Miltenburg[a,i], Ivo J. Huijbers[c], Marieke van de Ven[f], Jane E. Visvader[d,e], Geoffrey J. Lindeman[d,g,h], Lodewyk F. A. Wessels[b,l] and Jos Jonkers[a,i]

[a] Division of Molecular Pathology, The Netherlands Cancer Institute, Plesmanlaan 121, 1066 CX Amsterdam, The Netherlands
[b] Division of Molecular Carcinogenesis, The Netherlands Cancer Institute, 1066 CX Amsterdam, The Netherlands
[c] Transgenic Core Facility, Mouse Clinic for Cancer and Aging (MCCA), The Netherlands Cancer Institute, 1066 CX Amsterdam, The Netherlands
[d] ACRF Stem Cells and Cancer Division, Walter and Eliza Hall Institute of Medical Research, Parkville, Victoria 3052, Australia
[e] Department of Medical Biology, University of Melbourne, Parkville, Victoria 3010, Australia
[f] Preclinical Intervention Unit, Mouse Clinic for Cancer and Aging (MCCA), The Netherlands Cancer Institute, 1066 CX Amsterdam, The Netherlands
[g] Department of Medicine, University of Medicine, Parkville, VIC 3010, Australia
[h] Parkville Familial Cancer Centre, Royal Melbourne Hospital and Peter MacCallum Cancer Centre, Parkville, VIC 3050, Australia
[i] Cancer Genomics Netherlands, The Netherlands Cancer Institute, 1066 CX Amsterdam, The Netherlands
* The first four authors contributed equally to this work

Published in *Nature Communications*, 2019 Jan 23.

Abstract

BRCA1-mutated breast cancer is primarily driven by DNA copy-number alterations (CNAs) containing large numbers of candidate driver genes. Validation of these candidates requires novel approaches for high-throughput *in vivo* perturbation of gene function. We therefore developed genetically engineered mouse models (GEMMs) of BRCA1-deficient breast cancer that permit rapid introduction of putative drivers by either retargeting of GEMM-derived embryonic stem cells, lentivirus-mediated somatic overexpression or *in situ* CRISPR/Cas9-mediated gene disruption. We used these approaches to validate *Myc, Met, Pten* and *Rb1* as *bona fide* drivers in BRCA1-associated mammary tumorigenesis. Iterative mouse modeling and comparative oncogenomics analysis showed that MYC-overexpression strongly reshapes the CNA landscape of BRCA1-deficient mammary tumors and identified MCL1 as a collaborating driver in these tumors. Moreover, MCL1 inhibition potentiated the *in vivo* efficacy of PARP inhibition (PARPi), underscoring the therapeutic potential of this combination for treatment of *BRCA1*-mutated cancer patients with poor response to PARPi monotherapy.

Introduction

Triple-negative breast cancer (TNBC) accounts for 10%-15% of all breast cancers and is characterized by lack of expression of the estrogen receptor (ER), the progesterone receptor (PR) and the human epidermal growth factor receptor 2 (HER2). Due to the lack of these receptors, TNBCs cannot be treated with targeted therapies that have been effective in treating other breast cancer subtypes. As a result, TNBC has a relatively poor clinical prognosis and chemotherapy remains its current standard-of-care.

At the mutational level, TNBC is primarily a DNA copy-number driven disease (Ciriello *et al.,* 2013), harboring a multitude of copy-number alterations (CNAs) containing various driver genes (Cancer Genome Atlas, 2012). TNBCs are furthermore characterized by mutations in the *TP53* tumor suppressor gene, which occur in more than 80% of cases. Moreover, approximately 50% of TNBCs show loss of BRCA1 or BRCA2, either due to germline or somatic mutations or because of promoter hypermethylation (Cancer Genome Atlas, 2012). BRCA1 and BRCA2 are crucial for error-free repair of DNA double-strand breaks via homologous recombination, and loss of these genes results in high levels of chromosomal instability and a specific mutator phenotype. This results in recurrent patterns of CNAs in BRCA-deficient tumors, suggesting that these aberrations contain specific driver genes required for tumorigenesis.

Unfortunately, the high degree of genomic instability in BRCA-deficient TNBCs results in large numbers of CNAs harboring tens-to-thousands of genes, which complicates the identification of putative cancer drivers. To address this issue, several computational approaches have been developed to identify minimal regions that are recurrently gained or lost across tumors (Beroukhim *et al.,* 2007; Klijn *et al.,* 2008; van Dyk *et al.,* 2013; van Dyk *et al.,* 2016). Other approaches have complemented these tools with comparative oncogenomic strategies, in which combined analyses of human and mouse tumors are used to identify candidate driver genes that are frequently altered in tumors from both species (Zender *et al.,* 2006; Kim *et al.,* 2006; Mattison *et al.,* 2010). We have previously used comparative oncogenomics analyses to identify driver genes that were frequently aberrantly amplified or deleted in both mouse and human BRCA1-deficient TNBCs, including the proto-oncogene *MYC* and the tumor suppressor *RB1* (Holstege *et al.,* 2010). However, it is currently still unclear how exactly these putative drivers of BRCA1-deficient TNBC contribute to tumorigenesis, and specifically how they may influence the mutational landscape of the resulting tumors. To address these questions, we generated additional mouse models of BRCA1-deficient TNBC harboring different candidate genes. To overcome the time-consuming nature of generating these mouse models via germline engineering, we developed somatic mouse models of BRCA1-deficient TNBC and we showed that these models accurately reflect their germline

counterparts. We analyzed the resulting tumors to assess the contribution of candidate drivers to BRCA1-associated mammary tumorigenesis and to determine their effect on the copy-number landscape. Finally, by applying comparative oncogenomics to a combined set of germline and somatic BRCA1-deficient TNBCs with MYC overexpression, we identified MCL1 as a key driver and a therapeutic target in these tumors.

Results

Driver landscape in human BRCA1-deficient breast cancer

To determine the mutational landscape of human *BRCA1*-mutated breast cancer, we performed a meta-analysis by combining datasets from four large-scale breast cancer sequencing studies and extracting the mutational data of all *BRCA1*-mutated tumors. This analysis identified a total of 80 breast cancers (~1.5%) with a homozygous deletion or an inactivating (putative) driver mutation in *BRCA1* (Figure 1A, Supplementary Table 1). For 18 of these cases (~23%) triple-negative (TN) status could not be determined due to missing or inconclusive immunohistochemistry data. Of the remaining 62 cases, 40 (~65%) were scored as TNBC. Association with TN status was stronger in tumors from *BRCA1* germline mutations carriers (27/30) than in tumors with *BRCA1* somatic mutations (13/32).

We next analyzed the mutational landscape of the 80 BRCA1-deficient breast cancer cases, focusing on deleterious mutations, amplifications and homozygous deletions. At the mutational level, these tumors were mainly characterized by mutations in *TP53* (52/80, ~65%) and *PIK3CA* (23/80, ~29%). At the copy-number level, the most prominent events included amplifications of *MYC* (35/80, ~44%) and several co-amplified genes (e.g. *RAD21*, *EXT1*, *RECQL4*, *RSPO2*, *EPPK1*, *PLEC*) in the same locus (30-34%). MYC is a particularly well-known transcription factor that lies at the crossroad of several growth-promoting pathways and regulates global gene expression, resulting in increased proliferation and influencing many other cellular processes (reviewed in Meyer *et al.,* 2008 and Kress *et al.,* 2015). The *MYC* oncogene resides in the 8q24 genomic locus, which is among the most frequently amplified regions in breast cancer (Jain *et al.,* 2001), particularly in TNBC (Dillon *et al., 2016*). *MYC* expression and MYC signaling are aberrantly elevated in TNBC (Horiuchi *et al.,* 2012*;* Koboldt *et al.,* 2012) and a MYC transcriptional gene signature has been correlated with basal-like breast cancer (BLBC), a subtype typical for human BRCA1-deficient breast cancer (Alles *et al.*, 2009; Chandriani *et al.*, 2009; Gatza *et al.*, 2010). Altogether, this confirms that human BRCA1-deficient breast cancers are enriched for TNBCs and are mainly characterized by inactivating mutations in *TP53* and amplification of *MYC*.

MYC is a potent driver in BRCA1-associated mammary tumorigenesis

To study the contribution of MYC overexpression to BRCA1-associated mammary tumorigenesis, we initially employed the *K14Cre;Brca1*$^{F/F}$*;Trp53*$^{F/F}$ (KB1P) mouse model (Liu *et al.*, 2007), in which epithelium-specific loss of BRCA1 and p53 leads to the formation of mammary tumors and, to a lesser extent, other epithelial tumors including

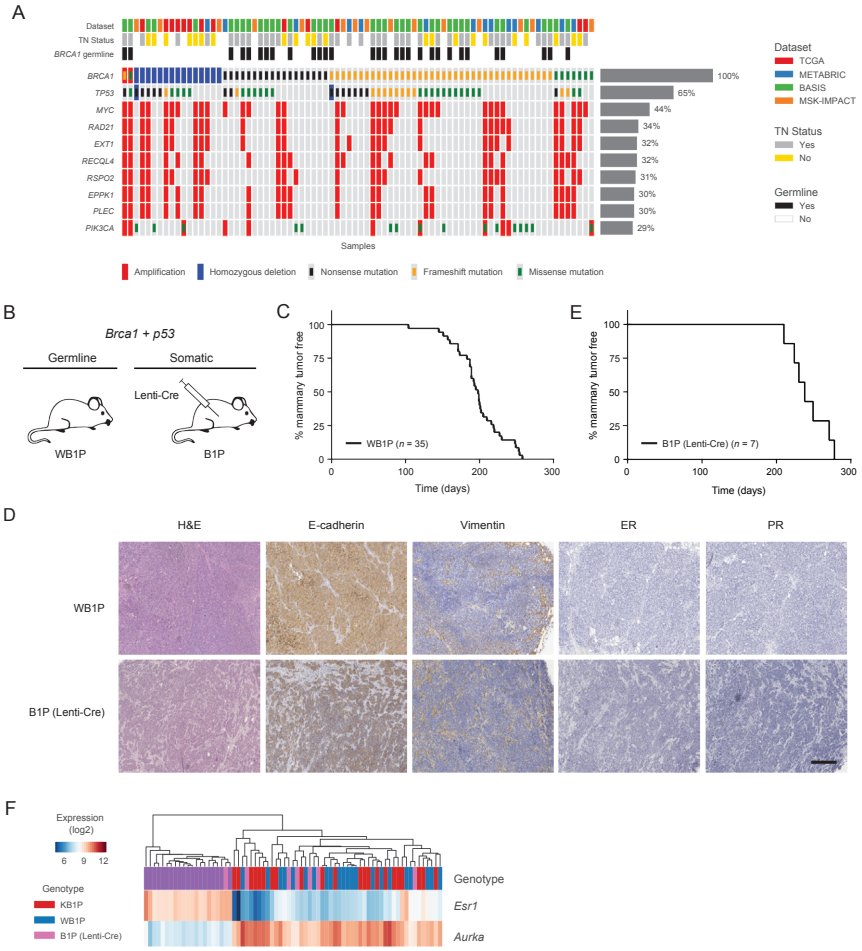

Figure 1 **Mutational landscape of human BRCA1-mutated TNBC and characterization of the WB1P model**. **(A)** Overview of the most common deleterious mutations and copy-number events in 80 *BRCA1*-mutated human breast tumor samples from four large-scale tumor-sequencing studies. **(B)** Overview of the germline and somatic mouse models for mammary gland-specific inactivation of conditional *Brca1* and *Trp53* alleles. **(C)** Kaplan-Meier curve showing mammary tumor-specific survival for *WapCre;Brca1*$^{F/F}$ *;Trp53*$^{F/F}$ (WB1P) female mice. **(D)** Representative hematoxylin and eosin (HE) staining and immunohistochemical detection of E-cadherin, vimentin, ER and PR in WB1P tumors and in tumors from Lenti-Cre injected *Brca1*$^{F/F}$*;Trp53*$^{F/F}$ (B1P) mice. Bar, 400 µm. **(E)** Kaplan-Meier curve showing mammary tumor-specific survival of B1P females injected with Lenti-Cre. **(F)** Unsupervised clustering (Euclidean distance, average linkage) of the WB1P tumors with tumors derived from published mouse models of luminal (*WapCre;Cdh1*$^{F/F}$*;Pten*$^{F/F}$, WEP; Boelens *et al.*, 2016) and basal-like (*K14Cre;Brca1*$^{F/F}$*;Trp53*$^{F/F}$, KB1P; Liu *et al.*, 2007) breast cancer, using a three-genes signature that distinguishes the PAM50 subtypes (Haibe-Kains *et al.*, 2012)

skin tumors. We used our previously established GEMM-ESC pipeline (Huijbers *et al.*, 2014) to generate *K14Cre;Brca1*$^{F/F}$*;Trp53*$^{F/F}$*;Col1a1*$^{invCAG\text{-}Myc\text{-}IRES\text{-}Luc/+}$ (KB1P-Myc) mice with epithelium-specific loss of BRCA1 and p53 and overexpression of MYC. Unfortunately, these mice were more prone to developing non-mammary tumors than KB1P mice and had to be sacrificed around 110 days for skin cancers and thymomas due to expression of K14Cre in these tissues.

To avoid unwanted development of non-mammary tumors, we took a two-pronged approach (Figure 1B). On one hand, we developed a novel GEMM (*WapCre;Brca1*$^{F/F}$*;Trp53*$^{F/F}$, WB1P) in which mammary-specific expression of Cre is driven by the whey acidic protein (*Wap*) gene promoter. In this WB1P model, female mice spontaneously developed mammary tumors with a median latency of 198 days (*n*=35, Figure 1C), which is comparable to the latency of KB1P females (median latency of 197 days, *n*=41). Similar to KB1P mammary tumors, WB1P tumors were either pure carcinomas (83%) or carcinosarcomas (17%). All tumors were poorly differentiated, negative for ER and PR (Figure 1D) and showed recombination of the *Brca1*^{F} and *Trp53*^{F} alleles. On the other hand, we employed a somatic strategy and performed intraductal injection of lentiviral vectors (Krause *et al.*, 2013; Rutkowski *et al.*, 2014; Tao *et al.*, 2016) expressing the Cre-recombinase (Lenti-Cre) in *Brca1*$^{F/F}$*;Trp53*$^{F/F}$ (B1P) females. Tumors from B1P mice injected with Lenti-Cre had a median latency of 238 days after injection (*n*=7, Figure 1E), and in terms of their morphology, they were indistinguishable from WB1P tumors (Figure 1D).

To determine if tumors from these two new mouse models reflected the basal-like subtype typical for human BRCA1-deficient breast cancer, we performed RNA-sequencing on 22 WB1P tumors and 7 tumors from B1P mice injected with Lenti-Cre, and compared their expression profile to tumors from the KB1P mouse model and a mouse model of luminal breast cancer (*WapCre;Cdh1*$^{F/F}$*;Pten*$^{F/F}$, WEP; Boelens *et al.*, 2016), using a three-gene signature that distinguishes the PAM50 subtypes (Haibe-Kains *et al.*, 2012). This analysis showed that all *Brca1*$^{\Delta/\Delta}$*;Trp53*$^{\Delta/\Delta}$ mouse mammary tumors from the three different mouse models cluster together and are characterized by low expression of *Esr1* and high expression of the proliferation marker *Aurka* (Figure 1F), reflecting the expression profile of human BLBC (Supplementary Figure 1A).

To study the effects of *Myc* amplification in WB1P mice, we applied the GEMM-ESC strategy (Huijbers *et al.*, 2014) to insert the conditional *invCAG-Myc-IRES-Luc* cassette into the *Col1a1* locus of WB1P embryonic stem cells (ESC). In the resulting *WapCre;Brca1*$^{F/F}$*;Trp53*$^{F/F}$*;Col1a1*$^{invCAG\text{-}Myc\text{-}IRES\text{-}Luc/+}$ (WB1P-Myc) model, mammary-specific expression of Cre induces inactivation of BRCA1 and p53 and concomitant overexpression of the MYC oncogene accompanied by luciferase expression (Figure 2A). WB1P-Myc female mice

developed multifocal mammary tumors with a median latency of 97 days (*n*=35, Figure 2B). These tumors grew exponentially (Supplementary Figure 2A) and animals had to be sacrificed 2-3 weeks after detection of palpable tumors. In contrast to the KB1P-Myc mice, WB1P-Myc mice developed only mammary tumors.

To test if somatic engineering could be used to overexpress MYC in the mammary gland, we performed intraductal injections of Lenti-Cre in *Brca1*$^{F/F}$;*Trp53*$^{F/F}$;*Col1a1*$^{invCAG\text{-}Myc\text{-}IRES\text{-}Luc/+}$ (B1P-Myc, *n*=16) females (Figure 2A). Moreover, we also injected lentiviral vectors encoding both Cre and *Myc* (Lenti-MycP2ACre, Supplementary Figure 3A) in B1P females (*n*=13) and lentiviral vectors encoding *Myc* (Lenti-Myc) in WB1P mice (*n*=15). Mice from all three groups developed mammary tumors with 100% penetrance and specifically in the injected glands (Figure 2C). B1P-Myc mice injected with Lenti-Cre developed tumors much faster than B1P mice injected with Lenti-Cre (126 days after injection vs 238 days after injection). B1P females injected with Lenti-MycP2ACre and WB1P females injected with Lenti-Myc developed tumors even faster (median latency of 92 and 61 days after injection, respectively), most likely due to higher *Myc* expression from the viral constructs than from the knock-in allele (Supplementary Figure 3B).

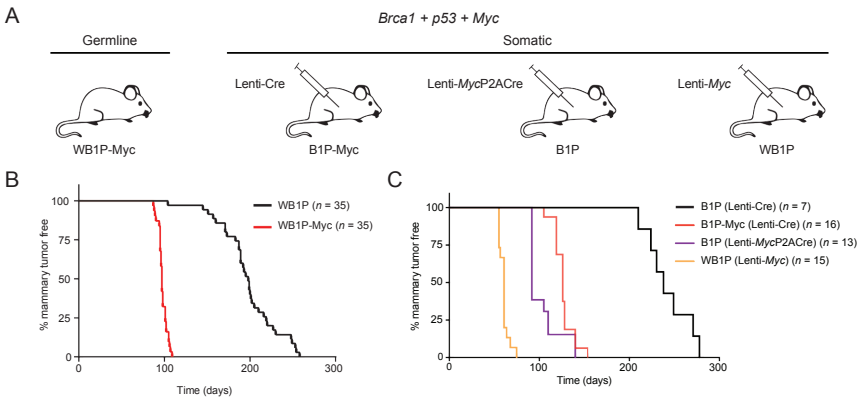

Figure 2 Validation of additional drivers in WB1P mice using germline and somatic engineering. (A) Overview of the germline and somatic mouse models for mammary gland-specific *Myc* overexpression in mice with conditional *Brca1* and *Trp53* alleles. (B) Kaplan-Meier curves showing mammary tumor-specific survival for the different genotypes. *WapCre;Brca1*$^{F/F}$;*Trp53*$^{F/F}$;*Col1a1*$^{invCAG\text{-}Myc\text{-}IRES\text{-}Luc/+}$ (WB1P-Myc*)* females showed a reduced mammary tumor-specific survival compared to WB1P littermates (97 days vs 198 days; ****$P < 0.0001$ by Mantel-Cox test). (C) Kaplan-Meier curves showing mammary tumor-specific survival for the different non-germline models. *Brca1*$^{F/F}$;*Trp53*$^{F/F}$;*Col1a1*$^{invCAG\text{-}Myc\text{-}IRES\text{-}Luc/+}$ (B1P-Myc*)* females injected with Lenti-Cre, B1P females injected with Lenti-MycP2ACre and WB1P females injected with Lenti-Myc showed a reduced mammary tumor-specific survival compared to B1P female mice injected with Lenti-Cre (respectively 126, 92 and 61 days after injection vs 238 days after injection; ****$P < 0.0001$ by Mantel-Cox test).

Histopathological analysis showed that, unlike the WB1P mouse model, WB1P-Myc females developed multifocal tumors that were all carcinomas. However, similar to WB1P tumors, WB1P-Myc tumors were poorly differentiated and ER-/PR-negative (Figure 2D). Furthermore, they displayed recombined *Brca1* and *Trp53* alleles and were sensitive to cisplatin and PARP inhibitors upon transplantation into nude mice (Supplementary Figure 2B). *WapCre;Brca1*$^{F/+}$*;Trp53*$^{F/F}$*;Col1a1*$^{invCAG\text{-}Myc\text{-}IRES\text{-}Luc/+}$ females that

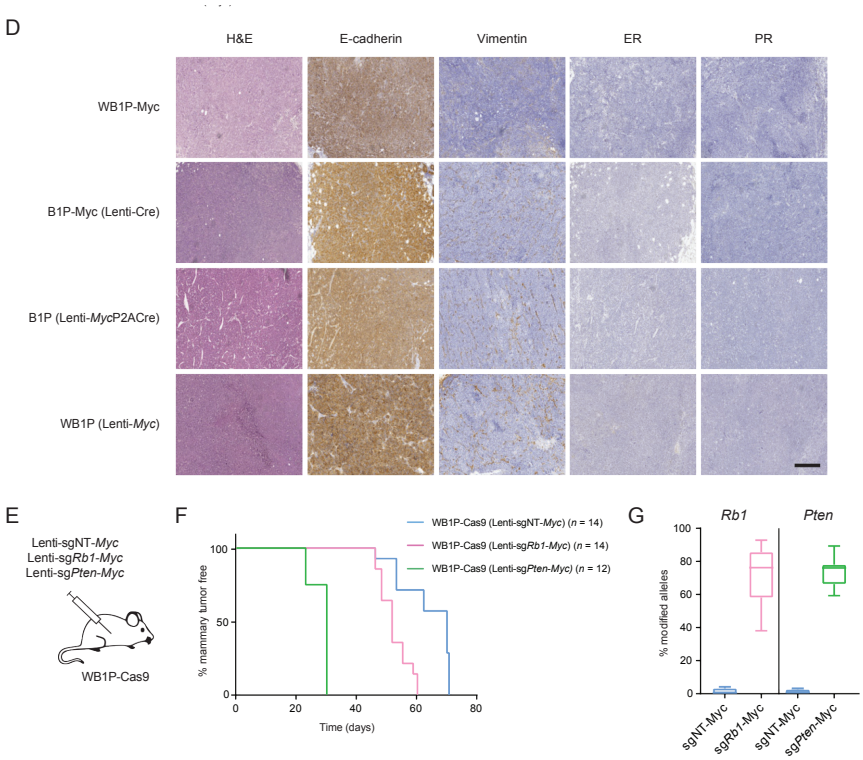

Figure 2 Continued. (D) Representative hematoxylin and eosin (HE) staining and immunohistochemical detection of E-cadherin, vimentin, ER and PR in tumors from WB1P-Myc females and in tumors from Lenti-Cre injected B1P-Myc mice, Lenti-MycP2ACre injected B1P mice and Lenti-Myc injected WB1P mice. Bar, 400 µm. (E) Overview of the intraductal injections performed in *WapCre;Brca1*$^{F/F}$*;Trp53*$^{F/F}$*;Col1a1*$^{invCAG\text{-}Cas9\text{-}IRES\text{-}Luc/+}$ (WB1P-Cas9) females with high-titer lentiviruses encoding *Myc* and either a non-targeting (NT) sgRNA (Lenti-sgNT-Myc), a sgRNA targeting exon 2 of *Rb1* (Lenti-sg*Rb1*-Myc) or a sgRNA targeting exon 7 of *Pten*. (F) Kaplan-Meier curves showing mammary tumor-specific survival for the different models. WB1P-Cas9 females injected with Lenti-sg*Pten*-Myc and *Lenti*-sg*Rb1*-Myc showed a reduced mammary tumor-specific survival compared to WB1P-Cas9 female mice injected with Lenti-sgNT-Myc (respectively 30 and 52 days after injection vs 70 days after injection, ****$P < 0.0001$ and ***$P < 0.001$ by Mantel-Cox test). (G) Boxplots depicting the fraction of modified *Rb1* and *Pten* alleles in tumors from WB1P-Cas9 mice injected with Lenti-sgNT-Myc, Lenti-sg*Rb1*-Myc and Lenti-sg*Pten*-Myc. Boxes extend from the third (Q3) to the first (Q1) quartile (interquartile range, IQR), with the line at the median; whiskers extend to Q3 + 1.5 × IQR and to Q1 − 1.5 × IQR.

were heterozygous for *Brca1*^{F} alleles (*n*=20) developed tumors slightly but significantly slower than *WapCre;Brca1*$^{F/F}$*;Trp53*$^{F/F}$*;Col1a1*$^{invCAG\text{-}Myc\text{-}IRES\text{-}Luc/+}$ mice with homozygous *Brca1*^{F} alleles (Supplementary Figure 2C). Histopathologic analysis showed that mammary tumors from the somatic models were indistinguishable from the cognate tumors from the germline models (Figure 2D). WB1P-Myc tumors showed similar expression levels of *Esr1* and *Aurka* as the WB1P tumors, indicating that they retained their basal-like subtype (Supplementary Figure 2D). Besides this, WB1P-Myc tumors showed high mRNA and protein levels of MYC compared to WB1P tumors, demonstrating successful expression of the knock-in allele (Supplementary Figure 2E-F). Unsupervised clustering of RNA-seq data from tumors from the somatic models confirmed that they also retained their basal-like phenotypes, and PCA analysis showed that these tumors also resemble their counterparts from the germline models in terms of their global gene expression profiles (Supplementary Figure 3C-E). Taken together, these data provide functional validation in germline and somatic models of the role of MYC in BRCA1-associated mammary tumorigenesis.

Loss of PTEN and RB1 collaborates with MYC in BRCA1-associated mammary tumorigenesis

After MYC amplification, the next most common alterations in our analysis of the human BRCA1-deficient TNBCs were mutations and/or amplifications of *PIK3CA* (23/80 cases), indicating that activation of PI3K signaling is an important driver in this breast cancer subtype (Figure 1A). Indeed, in addition to *PIK3CA* mutation/amplification, heterozygous or homozygous loss of *PTEN* (a negative regulator of PI3K signaling) was observed in 29/80 and 6/80 cases, respectively (Supplementary Table 1). Genetic alterations of *PIK3CA*/*PTEN* and *MYC* co-occurred in ~29% of all tumors analyzed (23/80 cases), indicating that MYC overexpression and PI3K pathway activation collaborate in BRCA1-related breast tumorigenesis.

To assess if activation of PI3K signaling via loss of PTEN collaborates with MYC overexpression in BRCA1-deficient TNBC, we developed *WapCre;Brca1*$^{F/F}$*;Trp53*$^{F/F}$*;Col1a1*$^{invCAG\text{-}Cas9\text{-}IRES\text{-}Luc/+}$ (WB1P-Cas9) mice with mammary-specific loss of BRCA1 and p53 and concomitant expression of Cas9. We then cloned and validated lentiviral vectors encoding a nontargeting sgRNA (sgNT) or a sgRNA targeting the seventh exon of *Pten* (sg*Pten*), in combination with a *Myc*-overexpression cassette. Since also RB1 loss has been implicated in BRCA1-deficient breast cancer (Kumar *et al.*, 2012) and MYC-driven TNBC (Knudsen *et al.*, 2015), we also generated a similar lentiviral vector encoding MYC and a sgRNA targeting the second exon of *Rb1* (sg*Rb1*). These lentiviral vectors (Lenti-sgNT-Myc, Lenti-sg*Pten*-Myc and Lenti-sg*Rb1*-Myc) were injected intraductally into WB1P-Cas9 females (Figure 2E) resulting in tumor formation with high penetrance

and very short latency (70, 30 and 52 days after injection, respectively; *n*=14,12 and 14, respectively, Figure 2F). Genomic DNA of mammary tumors from Lenti-sg*Pten*-Myc and Lenti-sg*Rb1*-Myc injected WB1P-Cas9 mice showed extensive modification of the target gene (Figure 2G; Supplementary Figure 4A-B), with a strong bias towards indels resulting in frameshift mutations, supporting homozygous inactivation of the tumor suppressor genes. Together, these results demonstrate that activation of PI3K signaling and RB1 loss collaborate with MYC in BRCA1-deficient TNBC.

MYC overexpression reshapes the copy-number landscape in BRCA1-deficient mammary tumors

To identify additional collaborating driver genes in BRCA1-deficient TNBC, we decided to characterize the CNA landscape of WB1P and WB1P-Myc tumors, with the assumption that recurrent CNAs in these tumors might underscore a conserved selective pressure towards the specific gain or loss of cancer genes that collaborate with loss of BRCA1 and p53 – alone or in combination with MYC overexpression – during TNBC development. We therefore performed DNA copy-number sequencing (CNV-seq) on 39 WB1P tumors and identified recurrent CNAs using RUBIC (van Dyk *et al.*, 2016). This analysis showed that WB1P tumors exhibit a high degree of genomic instability and harbor a multitude of recurrent gains and losses (Figure 3A; Supplementary Figure 5A). The most evident of these events was a focal amplification on chromosome 6 containing the *Met* oncogene. Besides *Met*, we also identified a recurrent loss on chromosome 14 (harboring *Rb1*) and several amplifications on chromosome 15 (containing *Myc*), in line with our previous studies in KB1P mice (Holstege *et al.*, 2010).

Remarkably, CNV-seq of 19 WB1P-Myc tumors showed a dramatically reshaped copy-number landscape (Figure 3B), with significantly fewer CNAs compared to the WB1P model (Figure 3C; $P < 0.00001$, two-sided Mann-Whitney U test). To determine if the decreased number of CNAs observed in WB1P-Myc tumors was not simply a result of the shortened tumor latency, we generated *WapCre;Brca1*$^{F/F}$*;Trp53*$^{F/F}$*;Col1a1*$^{invCAG\text{-}Met\text{-}IRES\text{-}Luc/+}$ (WB1P-Met) mice containing the *Met* oncogene, which we found frequently amplified in the WB1P tumors. Similar to WB1P-Myc females, WB1P-Met female mice developed multifocal mammary tumors with a short latency of 89 days (*n*=11, Supplementary Figure 6A). All WB1P-Met tumors were classified as poorly differentiated ER/PR-negative ductal carcinomas and showed MET overexpression and active MET signaling (Supplementary Figure 6B-E). These data confirm the previously reported role of MET in the onset and progression of TNBC (Knight *et al.*, 2013). CNV-sequencing of WB1P-Met tumors (*n*=20) showed an intermediate number of CNAs (Supplementary Figure 6F), which was lower than the WB1P tumors but significantly higher than the WB1P-Myc tumors ($P < 0.001$, one-sided Mann-Whitney U test). This demonstrates that

the observed differences in CNA load are not merely a function of tumor latency but also of the driver gene. Moreover, the validation of MET as a potent driver in BRCA1-associated tumorigenesis underscores the potential of iterative analysis of CNAs in progressively complex mouse models as an approach for identifying putative cancer genes that promote tumorigenesis in specific genetic contexts.

Comparative oncogenomics identifies MCL1 as a driver in BRCA1-deficient mammary tumors

Our RUBIC analyses showed that most of the CNAs identified in WB1P tumors were no longer present in WB1P-Myc tumors, suggesting an increased evolutionary pressure to acquire only specific driver mutations (Figure 3B). Interestingly, a small number of losses were retained, including the *Rb1*-associated loss on chromosome 14, further supporting

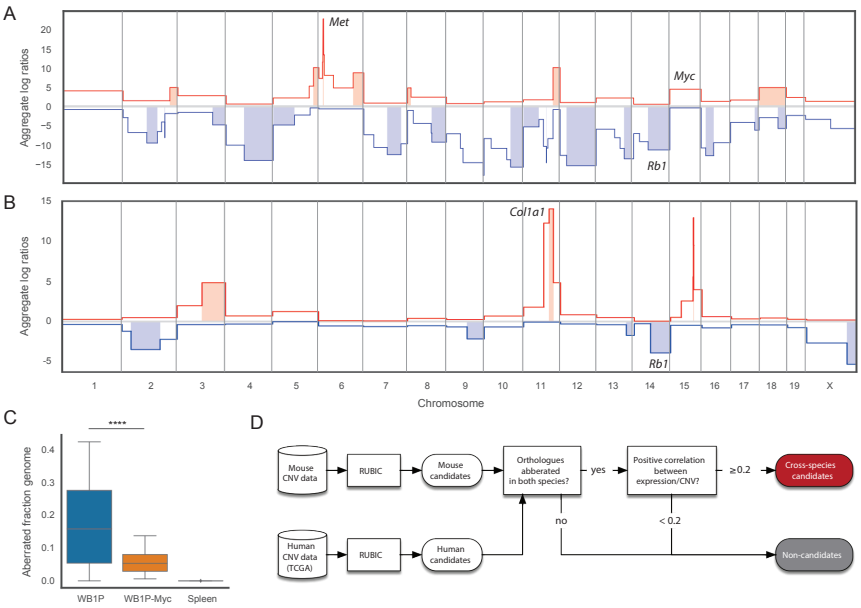

Figure 3 Identification of candidate drivers in WB1P-Myc tumors using comparative oncogenomics. (A-B) Genome-wide RUBIC analysis of CNV profiles of WB1P tumors (A) and WB1P-Myc tumors (B). Significant amplifications and deletions are marked by light red and blue columns, respectively. (C) Genomic instability of WB1P and WB1P-Myc tumors. Scores for spleen samples from WB1P mice are shown as reference; ****P < 0.0001 (two-sided Mann-Whitney U test). Boxes extend from the third (Q3) to the first (Q1) quartile (interquartile range, IQR), with the line at the median; whiskers extend to Q3 + 1.5 × IQR and to Q1 − 1.5 × IQR. See Materials and Methods for more details. (D) Flowchart illustrating the comparative oncogenomics analysis pipeline used for the identification of additional cancer driver genes.

Rb1 as a collaborating driver in MYC-driven BRCA1-deficient mammary tumors. Focusing on novel events, we identified a strongly recurrent amplicon on chromosome 11 encompassing the *Col1a1* locus in which we introduced the *invCAG-Myc-IRES-Luc* cassette. The recurrent amplification of this locus suggests that WB1P-Myc tumors underwent a selection for increased MYC expression via amplification of the conditional *Myc* knock-in allele. Besides this, we also identified novel recurrent amplifications on chromosome 3 and chromosome 15, which were syntenic with human 1q and 22q loci, respectively, which are commonly amplified in breast cancer patients.

To identify additional driver genes in MYC-driven BRCA1-deficient TNBC, we used a comparative oncogenomics strategy to select candidate genes that are recurrently aberrated in both WB1P-Myc tumors and human BLBCs from TCGA. In this approach (outlined in Figure 3D), we first identified candidate drivers in both species individually using RUBIC. For the mouse tumors, we combined CNV-seq data of tumors from both

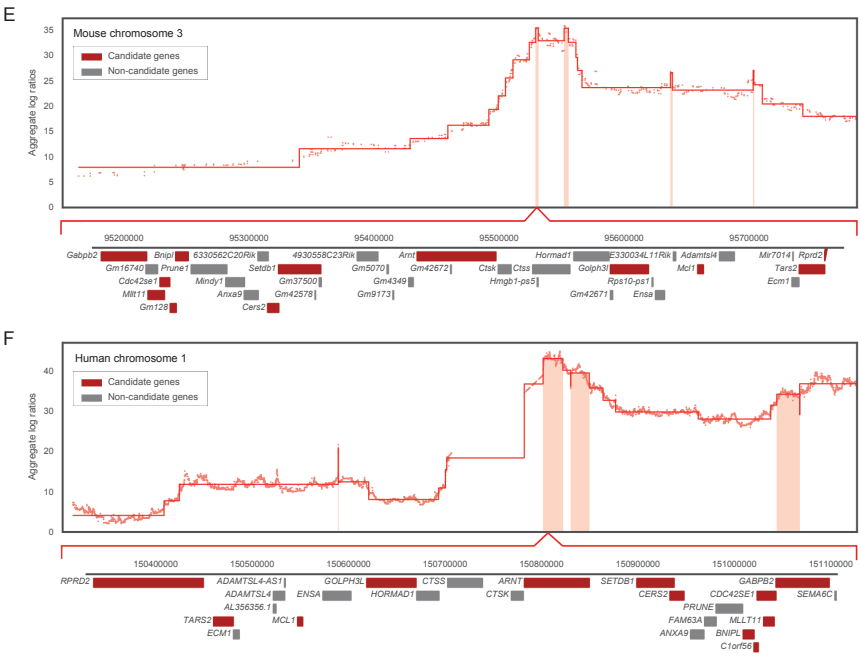

Figure 3 **Continued.** (E) Chromosome 3 RUBIC analysis of the combined CNV profiles of the tumors from germline and somatic mouse models overexpressing *Myc* in the mammary gland. Significant amplifications are marked by light red columns. Genes residing in the minimal amplicon of chromosome 3 are shown. Cross-species candidate genes surviving filter criteria are colored in red. (F) Chromosome 1 RUBIC analysis of the CNV profiles of human TNBC. Significant amplifications are marked by light red columns. Orthologs of the genes shown in panel E are shown. Cross-species candidate genes surviving filter criteria are colored in red.

the WB1P-Myc GEMM and the somatically engineered MYC-driven B1P models to increase our sample size, based on the observation that these tumors share the same distinctive CNA profile (Supplementary Figure 5B-C). Next, we mapped genes between species using mouse-human orthologs and took the intersection of both candidate lists. Finally, to prioritize genes that show differences in expression, we filtered the remaining candidates for genes with a positive Spearman correlation (> 0.2) between their expression and copy-number status.

After applying this strategy, we focused on genes residing in the recurrent amplifications on mouse chromosomes 3 and 15, as these were the most striking new events in the WB1P-Myc model. The recurrent amplification on chromosome 11 containing the conditional *Myc* knock-in allele in the *Col1a1* locus was excluded from this analysis. While this did not identify any candidate genes in the peak on chromosome 15 (mainly due to a lack of orthologous, recurrently aberrated genes), it did identify a list of 12 candidate genes residing in the peaks on mouse chromosome 3 (Figure 3E) and human

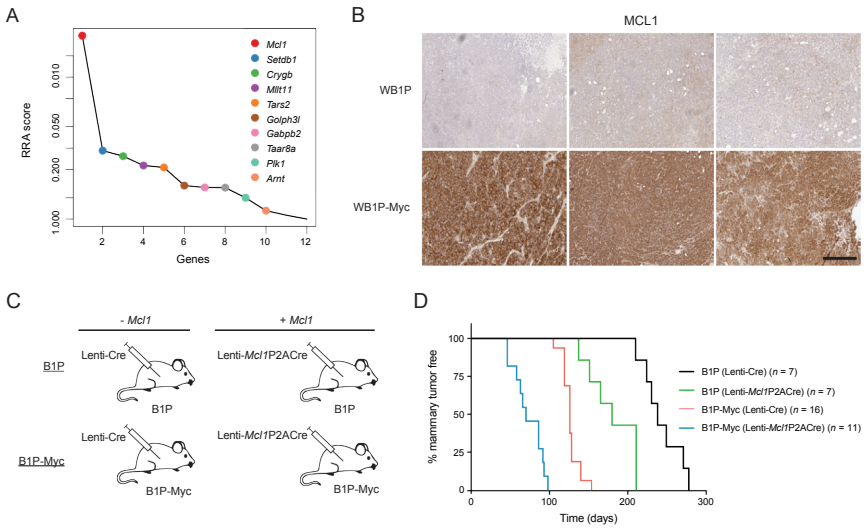

Figure 4 Validation of MCL1 as a druggable driver in *BRCA1*-mutated TNBC. (A) MAGeCK software was used to compute RRA scores for all genes included in our focused shRNA library, showing depletion of *Mcl1* shRNAs in WB1P-Myc organoids. (B) Immunohistochemical detection of MCL1 in multiple independent WB1P and WB1P-Myc tumors. Bar, 400 µm. (C) Overview of the non-germline mouse models for mammary-specific *Mcl1* overexpression. (D) Kaplan-Meier curves showing mammary tumor-specific survival for the different models. B1P and B1P-Myc females injected with Lenti-Mcl1P2ACre showed a reduced mammary tumor-specific survival compared to B1P and B1P-Myc female mice injected with Lenti-Cre, respectively (180 days after injection vs 238 days after injection; $^{**}P < 0.01$ by Mantel-Cox test; 70 days after injection vs 126 days after injection; $^{****}P < 0.0001$ by Mantel-Cox test).

chromosome 1q (Figure 3F). To identify potential drivers in this list of candidates, we derived organoids from a WB1P-Myc mammary tumor using our recently established methodology (Duarte *et al.*, 2017). We next performed a fitness screen in these WB1P-Myc organoids with a focused lentiviral shRNA library targeting candidate genes. This screen showed a marked depletion for shRNAs targeting *Mcl1* (Figure 4A), indicating that MCL1 expression is essential for growth of WB1P-Myc tumor cells. In line with this, WB1P-Myc tumors showed strongly elevated expression of MCL1 compared to WB1P tumors (Figure 4B).

To determine whether MCL1 cooperates with MYC in driving BRCA1-deficient TNBC, we generated a lentiviral vector encoding both *Cre* and *Mcl1* (Lenti-Mcl1P2ACre, Supplementary Figure 7A) and injected this lentivirus intraductally into B1P and B1P-Myc females (*n*=7 and *n*=11, respectively) to achieve simultaneous Cre-mediated recombination of the conditional alleles and overexpression of *Mcl1* (Figure 4C). Co-expression of MCL1 and Cre in B1P and B1P-Myc mice resulted in a significant

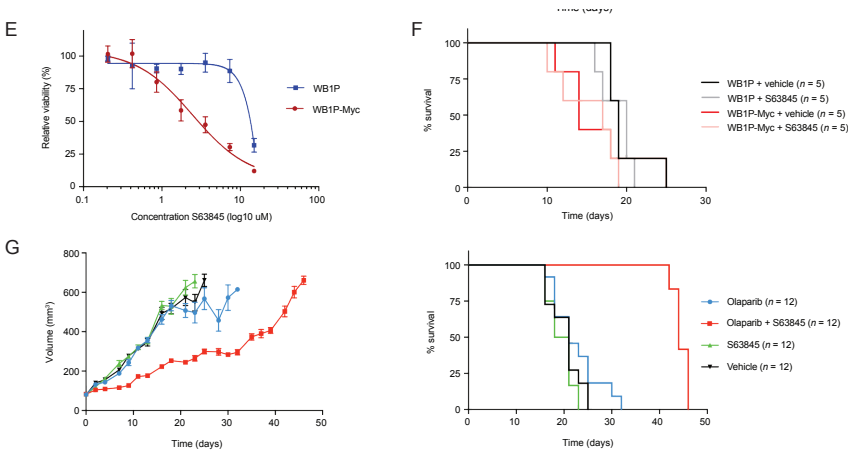

Figure 4 **Continued.** (E) *In vitro* response of WB1P and WB1P-Myc organoids to MCL1 inhibitor S63845. Error bars represent standard error of the mean. Experiment was performed in triplicate. (F) *In vivo* response of organoid-derived WB1P and WB1P-Myc tumors to S63845, as visualized by Kaplan-Meier curves. WB1P and WB1P-Myc organoid lines were transplanted in the fourth mammary fat pad of nude mice. When tumors had reached a size of 100 mm^3, mice were treated with 25 mg kg^{-1} S63845 (i.v. once-weekly for 5 weeks) or vehicle. (G) Response of the *BRCA1*-mutated TNBC PDX-110 xenograft model to S63845 and the PARP inhibitor olaparib, as visualized by tumor volume curves (left) and Kaplan-Meier curves (right). Single-cell suspensions of PDX-110 were transplanted in the fourth mammary fat pad of *NOD-SCID-IL2Rγ$_c^{-/-}$* mice. When tumors had reached a size of 100 mm^3, mice were treated with 25 mg kg^{-1} S63845 (i.v. once-weekly for 4 weeks), 50mg kg^{-1} olaparib (i.p. 5 days out of 7 for 4 weeks), both drugs or vehicle. Combination therapy with S63845 and olaparib prolonged survival compared to olaparib monotherapy (****$P < 0.0001$ by Mantel-Cox test). Error bars represent standard error of the mean.

decrease in tumor latency compared to mice in which only Cre was delivered (180 vs 238 days and 70 vs 126 days, respectively; Figure 4D; Supplementary Figure 7B). MCL1 overexpression appeared to relieve pressure for chromosome 3 amplification in the resulting tumors (Supplementary Figure 7C-D). Conversely, MCL1 silencing in WB1P-Myc organoids resulted in *Myc* downregulation (Supplementary Figure 7E). Altogether, these analyses identify *Mcl1* as an important driver gene in the recurrent amplification on mouse chromosome 3 and demonstrate that MCL1 effectively collaborates with MYC in BRCA1-associated breast tumorigenesis.

MCL1-inhibition synergizes with PARP-inhibition in a patient-derived xenograft model of BRCA1-mutated TNBC

Our focused shRNA library screen showed that knockdown of *Mcl1* is detrimental to WB1P-Myc organoids. To test whether WB1P-Myc tumors are also sensitive to pharmacological MCL1-inhibition, we tested the *in vitro* sensitivity of WB1P and WB1P-Myc organoids to the selective MCL1 inhibitor S63845 (Kotschy *et al.*, 2016), which was recently shown to display activity in patient-derived xenograft (PDX) models of breast cancer (Merino *et al.*, 2017). In contrast to other BH3 mimetics, S63845 binds to human MCL1 at sub-nanomolar concentrations whereas it does not display detectable binding to other anti-apoptotic family members (Kotschy *et al.*, 2016). Proliferation assays indicated that WB1P-Myc organoids were more sensitive to S63845 than WB1P organoids (Figure 4E). To examine the response of WB1P and WB1P-Myc tumors to MCL1-inhibition, we transplanted WB1P and WB1P-Myc organoids orthotopically into nude mice (n=10 per line) and tested the response of the tumor outgrowths to S63845. However, in this setting we did not observe a differential sensitivity to MCL1-inhibition, as none of the tumors responded to S63845 at the tested dose (Figure 4F).

Based on the anti-apoptotic role of MCL1, we reasoned that MCL1-inhibition might be most effective when combined with a pro-apoptotic drug, as previously demonstrated in PDX models of HER2-amplified breast cancer and TNBC treated with trastuzumab and docetaxel, respectively (Merino *et al.*, 2017). We therefore investigated whether S63845 could enhance the efficacy of the clinical PARP inhibitor (PARPi) olaparib, which is currently used for treatment of *BRCA1*-mutated breast cancer patients. As the olaparib-sensitivity of WB1P and WB1P-Myc tumors was too high to assess any synergistic effect of MCL1-inhibition (Supplementary Figure 2B; Supplementary Figure 8A-B), we turned to a PDX model of *BRCA1*-mutated TNBC (PDX-110), which expresses relatively high levels of MYC and MCL1 and shows limited sensitivity to PARPi (Merino *et al.*, 2017). To assess the effect of combined inhibition of PARP and MCL1 in this model, PDX tumor cells were orthotopically injected into *NOD-SCID-IL2R*$\gamma_c^{-/-}$ mice (n=48), which were randomly allocated to vehicle-, single- or double-treatment arms once tumors

reached a volume of 100 mm^3. Remarkably, while treatment with S63845 or olaparib alone did not elicit a clinical response, tumor growth was considerably inhibited upon treatment with both drugs and tumors relapsed only when treatment was stopped after 4 weeks (Figure 4G).

Discussion

In this work, we have used both germline and somatic engineering approaches to rapidly test candidate cancer drivers in the WB1P mouse model of BRCA1-deficient TNBC. Using this approach, we validated MYC, MET, PTEN and RB1 as bona fide drivers of BRCA1-associated tumorigenesis and showed that MYC overexpression dramatically changes the mutational landscape of the resulting tumors. Finally, by applying a comparative oncogenomics strategy to uncover additional culprits of tumorigenesis, we identified MCL1 as a druggable cancer driver that collaborates with MYC in BRCA1-deficient TNBC. An important challenge of modeling cancer in mice, is that it requires technology that allows rapid introduction of new driver mutations to quickly create a variety of compound-mutant mouse models containing different combinations of candidate genes. Such experiments are difficult to perform using germline engineering approaches, which generally involve extensive cross-breeding of single-mutant mice to produce animals carrying the desired combination of mutations. Here, we have shown that somatic engineering using lentiviral vectors for overexpression of cDNAs and CRISPR-mediated *in situ* gene editing provides an effective alternative for rapid generation of novel mouse models of BRCA1-deficient TNBC. The limitations of cDNA-based overexpression systems – which may not fully recapitulate the desired expression levels of candidate genes – might be alleviated by implementing novel technologies for CRISPR-mediated transcriptional control (CRISPRi/CRISPRa) and base-editing of endogenous genes. We therefore expect that our somatic engineering methodology can ultimately be used to generate refined breast cancer models containing a wide variety of fine-tuned (epi) genetic permutations.

One of the key advantages of this type of iterative mouse modeling, is that it highlights the profound effect that additional driver genes can have on the mutational landscape of a baseline tumor model. This indicates that the evolutionary pressure that tumor cells experience depends strongly on the combination of driver mutations, which push cells down a specific path to acquire additional aberrations that most effectively collaborate with the pre-existing events. This notion has two important implications. First, it means that it is crucial to study driver genes in the appropriate genetic contexts as observed in human tumors, as they may have very different effects in different backgrounds. Second, predominant changes in the mutational landscape likely indicate that the pre-existing driver(s) push tumors down a relatively restricted evolutionary path, which might be exploited therapeutically.

A clear example is provided by our study, showing that MYC-overexpression pushes the evolution of BRCA1-deficient TNBC towards amplification of a druggable driver, MCL1. Although MYC is a potent inducer of cell proliferation, supraphysiologic overexpression

of *MYC* also has pro-apoptotic effects and is generally not tolerated in non-transformed cells (Meyer *et al.*, 2006). This suggests that tumor cells need to acquire additional alterations in other, collaborating cancer driver genes to counteract MYC-induced apoptosis. MCL1 belongs to the Bcl-2 family and is involved in the inhibition of apoptosis (Clohessy *et al.*, 2006). While it cannot be excluded that MYC overexpression reshapes evolution of BRCA1-deficient TNBCs via negative selection of tumor cell clones with high levels of CNAs, amplifications of *MCL1* might be particularly selected for as they may counteract the pro-apoptotic effects of MYC overexpression. *MCL1* amplifications have been identified in a variety of tumor types, including breast cancer (Beroukhim *et al.*, 2010), where they correlate with poor survival (Ding *et al.*, 2007; Campbell *et al.*, 2018). Although the commonly amplified chromosome 1q region (where *MCL1* resides) might harbor additional driver genes, MCL1 is the main pro-survival protein upregulated in TNBC (Goodwin *et al.*, 2015), and amplification of *MCL1* has been implicated in resistance to multiple therapies used in patients with TNBC, where it is often co-amplified with *MYC* (Balko *et al.*, 2014; Lee *et al.*, 2017). We found amplification of *MCL1* in 15% of the *BRCA1*-mutated TNBCs we analyzed (12/80 cases), and two-thirds of these cases showed co-amplification of *MYC* (Supplementary Figure 8C). MCL1 and MYC were also shown to cooperate in mouse models of leukemia and non-small cell lung cancer (NSCLC), and co-expression of these two factors correlates with poor NSCLC patient survival (Xiang *et al.*, 2010; Allen *et al.*, 2011). This suggests that MCL1 inhibition might be particularly effective against *MYC*-overexpressing tumors by exposing them to MYC-induced apoptosis. MCL1 has only recently been recognized as an important therapeutic target, and currently several MCL1 inhibitors are being tested in preclinical trials, where they are showing promising activity, especially in combination therapies (Merino *et al.*, 2017; Mitchell *et al.*, 2010). Five phase-I clinical trials are currently ongoing for testing MCL1 inhibitors in patients with hematopoietic malignancies (NCT02675452; NCT02992483; NCT02979366; NCT03672695; NCT03465540). Our study demonstrates that MCL1 inhibition considerably enhances response of *BRCA1*-mutated TNBC to the clinical PARPi olaparib and suggests that this combination should be prioritized for clinical evaluation, especially in *BRCA1*-mutated cancer patients with poor response to PARPi monotherapy.

Another example of identification of druggable drivers in mouse models of BRCA1-deficient TNBC was recently provided by Liu *et al.* (Liu *et al.*, 2018), who analyzed transcriptional and CNA profiles of mammary tumors from our previously published KB1P and *K14Cre;Trp53*$^{F/F}$ (KP) models (Liu *et al.*, 2007). This analysis yielded a spectrum of somatic genetic alterations putatively driving tumor evolution, including gene-fusions and chromosomal amplifications and deletions (including recurrent amplification of *Met* and *Myc* and deletion of *Rb1*). Interestingly, even though KB1P and KP tumors were following diverse evolutionary trajectories, most tumors displayed enhanced activation

of MAPK and/or PI3K signaling and could be treated with inhibitors specific for the aberrated drug target.

In summary, we applied novel germline and somatic technologies to functionally validate the role of candidate drivers in BRCA1-deficient TNBC *in vivo* at unprecedented speed. Our integrate approach revealed a profound effect of MYC overexpression on tumor evolution and identified MCL1 as a critical and druggable dependency in BRCA1-deficient TNBC with high expression of MYC. Combined inhibition of MCL1 and PARP might benefit a subset of *BRCA1*-mutated TNBC patients and warrants further investigation.

Acknowledgments

We thank Sjors Kas, Eva Schut, Bastiaan Evers, Ben Morris, Renske de Korte-Grimmerink, Natalie Proost and Rebecca Theeuwsen for providing reagents, technical suggestions, and/or help with the experiments. We are grateful for excellent support from the NKI animal facility, RHPC computing facility, flow cytometry facility, animal pathology facility, transgenic facility, preclinical intervention unit, core facility molecular pathology and biobanking (CFMPB), and genomics core facility. PDX-110 was derived from a primary breast tumor provided by the Victorian Cancer Biobank (supported by the Victorian Government, Australia). This work was carried out on the Dutch national e-infrastructure with the support of SURF Cooperative (e-infra160136). Financial support was provided by the Netherlands Organization for Scientific Research (NWO: Cancer Genomics Netherlands (CGCNL), Cancer Systems Biology Center (CSBC), Netherlands Genomics Initiative (NGI) Zenith 93512009 (J.J.), VICI 91814643 (J.J.)), the European Research Council (ERC Synergy project CombatCancer), a National Roadmap grant for Large-Scale Research Facilities from NWO (J.J.) and National Health and Medical Research Council (Australia) grants 1113133 (J.E.V. and G.J.L.), 1078730 (G.J.L.) and 1102742 (J.E.V.).

Author contributions

Conceived the study: S.A., J.R.d.R., L.H., C.S.B., L.F.A.W., J.J.. Designed and supervised the experiments: S.A., J.R.d.R., L.H., C.S.B., F.V., M.H.v.M., I.J.H., M.v.d.V., J.E.V., G.J.L., L.F.A.W., J.J.. Performed the experiments: S.A., J.R.d.R., L.H., C.S.B., C.L., F.V., F.F., A.D., E.v.d.B., B.S., B.v.G., R.d.B., M.H.v.M.. Analyzed and interpreted data: S.A., J.R.d.R., L.H., C.S.B., F.V., J.E.V., G.J.L., L.F.A.W., J.J.. Wrote the paper: S.A., J.R.d.R., J.J..

References

Allen TD, Zhu CQ, Jones KD, Yanagawa N, Tsao MS, Bishop JM. Interaction between MYC and MCL1 in the genesis and outcome of non-small-cell lung cancer. Cancer Res 2011;71:2212-21

Alles MC, Gardiner-Garden M, Nott DJ, Wang Y, Foekens JA, Sutherland RL, et al. Meta-analysis and gene set enrichment relative to er status reveal elevated activity of MYC and E2F in the “basal” breast cancer subgroup. PLoS One 2009;4:e4710

Annunziato S, Kas SM, Nethe M, Yucel H, Del Bravo J, Pritchard C, et al. Modeling invasive lobular breast carcinoma by CRISPR/Cas9-mediated somatic genome editing of the mammary gland. Genes Dev 2016;30:1470-80

Balko JM, Giltnane JM, Wang K, Schwarz LJ, Young CD, Cook RS, et al. Molecular profiling of the residual disease of triple-negative breast cancers after neoadjuvant chemotherapy identifies actionable therapeutic targets. Cancer Discov 2014;4:232-45

Beroukhim R, Getz G, Nghiemphu L, Barretina J, Hsueh T, Linhart D, et al. Assessing the significance of chromosomal aberrations in cancer: methodology and application to glioma. Proc Natl Acad Sci U S A 2007;104:20007-12

Beroukhim R, Mermel CH, Porter D, Wei G, Raychaudhuri S, Donovan J, et al. The landscape of somatic copy-number alteration across human cancers. Nature 2010;463:899-905

Boelens MC, Nethe M, Klarenbeek S, de Ruiter JR, Schut E, Bonzanni N, et al. PTEN Loss in E-Cadherin-Deficient Mouse Mammary Epithelial Cells Rescues Apoptosis and Results in Development of Classical Invasive Lobular Carcinoma. Cell Rep 2016;16:2087-101

Brinkman EK, Chen T, Amendola M, van Steensel B. Easy quantitative assessment of genome editing by sequence trace decomposition. Nucleic Acids Res 2014;42:e168

Cancer Genome Atlas N. Comprehensive molecular portraits of human breast tumours. Nature 2012;490:61-70

Campbell KJ, Dhayade S, Ferrari N, Sims AH, Johnson E, Mason SM, et al. MCL-1 is a prognostic indicator and drug target in breast cancer. *Cell Death Dis* 2018;9:19

Chandriani S, Frengen E, Cowling VH, Pendergrass SA, Perou CM, Whitfield ML, et al. A core MYC gene expression signature is prominent in basal-like breast cancer but only partially overlaps the core serum response. PLoS One 2009;4:e6693

Ciriello G, Miller ML, Aksoy BA, Senbabaoglu Y, Schultz N, Sander C. Emerging landscape of oncogenic signatures across human cancers. Nat Genet 2013;45:1127-33

Clohessy JG, Zhuang J, de Boer J, Gil-Gomez G, Brady HJ. Mcl-1 interacts with truncated Bid and inhibits its induction of cytochrome c release and its role in receptor-mediated apoptosis. J Biol Chem 2006;281:5750-9

Derksen PW, Liu X, Saridin F, van der Gulden H, Zevenhoven J, Evers B, et al. Somatic inactivation of E-cadherin and p53 in mice leads to metastatic lobular mammary carcinoma through induction of anoikis resistance and angiogenesis. Cancer Cell 2006;10:437-49

Dillon JL, Mockus SM, Ananda G, Spotlow V, Wells WA, Tsongalis GJ, et al. Somatic gene mutation analysis of triple negative breast cancers. Breast 2016;29:202-7

Ding Q, He X, Xia W, Hsu JM, Chen CT, Li LY, et al. Myeloid cell leukemia-1 inversely correlates with glycogen synthase kinase-3beta activity and associates with poor prognosis in human breast cancer. Cancer Res 2007;67:4564-71

Doornebal CW, Klarenbeek S, Braumuller TM, Klijn CN, Ciampricotti M, Hau CS, et al. A preclinical mouse model of invasive lobular breast cancer metastasis. Cancer Res 2013;73:353-63

Duarte AA, Gogola E, Sachs N, Barazas M, Annunziato S, J RdR, et al. BRCA-deficient mouse mammary tumor organoids to study cancer-drug resistance. Nat Methods 2018;15:134-40

Evers B, Jastrzebski K, Heijmans JP, Grernrum W, Beijersbergen RL, Bernards R. CRISPR knockout screening outperforms shRNA and CRISPRi in identifying essential genes. Nat Biotechnol 2016;34:631-3

Follenzi A, Ailles LE, Bakovic S, Geuna M, Naldini L. Gene transfer by lentiviral vectors is limited by nuclear translocation and rescued by HIV-1 pol sequences. Nat Genet 2000;25:217-22

Gatza ML, Lucas JE, Barry WT, Kim JW, Wang Q, Crawford MD, et al. A pathway-based classification of human breast cancer. Proc Natl Acad Sci U S A 2010;107:6994-9

Goodwin CM, Rossanese OW, Olejniczak ET, Fesik SW. Myeloid cell leukemia-1 is an important apoptotic survival factor in triple-negative breast cancer. Cell Death Differ 2015;22:2098-106

Haibe-Kains B, Desmedt C, Loi S, Culhane AC, Bontempi G, Quackenbush J, et al. A three-gene model to robustly identify breast cancer molecular subtypes. J Natl Cancer Inst 2012;104:311-25

Henneman L, van Miltenburg MH, Michalak EM, Braumuller TM, Jaspers JE, Drenth AP, et al. Selective resistance to the PARP inhibitor olaparib in a mouse model for BRCA1-deficient metaplastic breast cancer. Proc Natl Acad Sci U S A 2015;112:8409-14

Holstege H, van Beers E, Velds A, Liu X, Joosse SA, Klarenbeek S, et al. Cross-species comparison of aCGH data from mouse and human BRCA1- and BRCA2-mutated breast cancers. BMC Cancer 2010;10:455

Horiuchi D, Kusdra L, Huskey NE, Chandriani S, Lenburg ME, Gonzalez-Angulo AM, et al. MYC pathway activation in triple-negative breast cancer is synthetic lethal with CDK inhibition. J Exp Med 2012;209:679-96

Huijbers IJ, Bin Ali R, Pritchard C, Cozijnsen M, Kwon MC, Proost N, et al. Rapid target gene validation in complex cancer mouse models using re-derived embryonic stem cells. EMBO Mol Med 2014;6:212-25

Jain AN, Chin K, Borresen-Dale AL, Erikstein BK, Eynstein Lonning P, Kaaresen R, et al. Quantitative analysis of chromosomal CGH in human breast tumors associates copy number abnormalities with p53 status and patient survival. Proc Natl Acad Sci U S A 2001;98:7952-7

Kas SM, de Ruiter JR, Schipper K, Annunziato S, Schut E, Klarenbeek S, et al. Insertional mutagenesis identifies drivers of a novel oncogenic pathway in invasive lobular breast carcinoma. Nat Genet 2017;49:1219-30

Kim M, Gans JD, Nogueira C, Wang A, Paik JH, Feng B, et al. Comparative oncogenomics identifies NEDD9 as a melanoma metastasis gene. Cell 2006;125:1269-81

Klijn C, Holstege H, de Ridder J, Liu X, Reinders M, Jonkers J, et al. Identification of cancer genes using a statistical framework for multiexperiment analysis of nondiscretized array CGH data. Nucleic Acids Res 2008;36:e13

Knight JF, Lesurf R, Zhao H, Pinnaduwage D, Davis RR, Saleh SM, et al. Met synergizes with p53 loss to induce mammary tumors that possess features of claudin-low breast cancer. Proc Natl Acad Sci U S A. 2013;110:E1301-10.

Knudsen ES, McClendon AK, Franco J, Ertel A, Fortina P, Witkiewicz AK. RB loss contributes to aggressive tumor phenotypes in MYC-driven triple negative breast cancer. Cell Cycle 2015;14:109-22

Koboldt DC, Zhang Q, Larson DE, Shen D, McLellan MD, Lin L, et al. VarScan 2: somatic mutation and copy number alteration discovery in cancer by exome sequencing. Genome Res 2012;22:568-76

Kotschy A, Szlavik Z, Murray J, Davidson J, Maragno AL, Le Toumelin-Braizat G, et al. The MCL1 inhibitor S63845 is tolerable and effective in diverse cancer models. Nature 2016;538:477-82

Krause S, Brock A, Ingber DE. Intraductal injection for localized drug delivery to the mouse mammary gland. J Vis Exp 2013

Kress TR, Sabo A, Amati B. MYC: connecting selective transcriptional control to global RNA production. Nat Rev Cancer 2015;15:593-607

Kumar P, Mukherjee M, Johnson JP, Patel M, Huey B, Albertson DG, et al. Cooperativity of Rb, Brca1, and p53 in malignant breast cancer evolution. PLoS Genet 2012;8:e1003027

Lee KM, Giltnane JM, Balko JM, Schwarz LJ, Guerrero-Zotano AL, Hutchinson KE, et al. MYC and MCL1 Cooperatively Promote Chemotherapy-Resistant Breast Cancer Stem Cells via Regulation of Mitochondrial Oxidative Phosphorylation. Cell Metab 2017;26:633-47 e7

Liu X, Holstege H, van der Gulden H, Treur-Mulder M, Zevenhoven J, Velds A, et al. Somatic loss of BRCA1 and p53 in mice induces mammary tumors with features of human BRCA1-mutated basal-like breast cancer. Proc Natl Acad Sci U S A 2007;104:12111-6

Liu H, Murphy CJ, Karreth FA, Emdal KB, White FM, Elemento O, et al. Identifying and targeting sporadic oncogenic genetic aberrations in mouse models of triple-negative breast cancer. Cancer Discov 2018;8:354-69.

Mattison J, Kool J, Uren AG, de Ridder J, Wessels L, Jonkers J, et al. Novel candidate cancer genes identified by a large-scale cross-species comparative oncogenomics approach. Cancer Res 2010;70:883-95

Merino D, Whittle JR, Vaillant F, Serrano A, Gong JN, Giner G, et al. Synergistic action of the MCL-1 inhibitor S63845 with current therapies in preclinical models of triple-negative and HER2-amplified breast cancer. Sci Transl Med 2017;9

Meyer N, Kim SS, Penn LZ. The Oscar-worthy role of Myc in apoptosis. Semin Cancer Biol 2006;16:275-87

Meyer N, Penn LZ. Reflecting on 25 years with MYC. Nat Rev Cancer 2008;8:976-90

Mitchell C, Yacoub A, Hossein H, Martin AP, Bareford MD, Eulitt P, et al. Inhibition of MCL-1 in breast cancer cells promotes cell death in vitro and in vivo. Cancer Biol Ther 2010;10:903-17

Nik-Zainal S, Davies H, Staaf J, Ramakrishna M, Glodzik D, Zou X, et al. Landscape of somatic mutations in 560 breast cancer whole-genome sequences. Nature 2016;534:47-54

Rutkowski MR, Allegrezza MJ, Svoronos N, Tesone AJ, Stephen TL, Perales-Puchalt A, et al. Initiation of metastatic breast carcinoma by targeting of the ductal epithelium with adenovirus-cre: a novel transgenic mouse model of breast cancer. J Vis Exp 2014

Sanjana NE, Shalem O, Zhang F. Improved vectors and genome-wide libraries for CRISPR screening. Nat Methods 2014;11:783-4

Tao L, van Bragt MP, Laudadio E, Li Z. Lineage tracing of mammary epithelial cells using cell-type-specific cre-expressing adenoviruses. Stem Cell Reports 2014;2:770-9

van Dyk E, Reinders MJ, Wessels LF. A scale-space method for detecting recurrent DNA copy number changes with analytical false discovery rate control. Nucleic Acids Res 2013;41:e100

van Dyk E, Hoogstraat M, Ten Hoeve J, Reinders MJ, Wessels LF. RUBIC identifies driver genes by detecting recurrent DNA copy number breaks. Nat Commun 2016;7:12159

Xiang Z, Luo H, Payton JE, Cain J, Ley TJ, Opferman JT, et al. Mcl1 haploinsufficiency protects mice from Myc-induced acute myeloid leukemia. J Clin Invest 2010;120:2109-18

Zender L, Spector MS, Xue W, Flemming P, Cordon-Cardo C, Silke J, et al. Identification and validation of oncogenes in liver cancer using an integrative oncogenomic approach. Cell 2006;125:1253-67

Materials and Methods

Lentiviral vectors

The Lenti-Cre vector (pBOB-CAG-iCRE-SD, Addgene plasmid #12336) was a kind gift of Lorenzo Bombardelli. Lenti-MycP2Acre and Lenti-Mcl1-P2Acre were cloned as follows. AgeI and SalI were used to remove GFP-T2A-puro from the SIN.LV.SF-GFP-T2A-puro (Kas *et al.*, 2017). P2Acre was synthesized with AgeI-SalI overhangs and inserted as AgeI-SalI fragment into the SIN.LV.SF-GFP-T2A-puro backbone, resulting in SIN.LV.SF-P2A-Cre. *Myc* and *Mcl1* murine cDNAs were isolated with BamHI-AgeI overhangs using standard PCR from cDNA clones (Clone 8861953, Source BioScience; Clone 3491015, Dharmacon) and inserted as BamHI-AgeI fragments into the SIN. LV.SF-P2A-Cre vector. The Lenti-sg*Rb1*-Myc, Lenti-sg*Pten*-Myc and Lenti-sgNT-Myc vectors were cloned as follows. *Myc* cDNA was isolated with XbaI-XhoI overhangs using standard PCR from the Lenti-MycP2Acre vector, and inserted as XbaI-XhoI fragment into pGIN, a lentiviral vector for sgRNA overexpression (Evers *et al.*, 2016). The non-targeting sgRNA (TGATTGGGGGTCGTTCGCCA) and sgRNAs targeting mouse *Rb1* exon 2 (TCTTACCAGGATTCCATCCA) and mouse *Pten* exon 7 (CCTCAGCCATTGCCTGTGTG) were cloned as described (Sanjana *et al.*, 2014). All vectors were validated by Sanger sequencing. Concentrated stocks of VSV-G pseudotyped lentivirus were produced by transient co-transfection of four plasmids in 293T as previously described (Follenzi *et al.*, 2000). Lentiviral titers were determined using the qPCR lentivirus titration kit from Abm (LV900).

Cell culture

293T cells for lentiviral production and Cre-reporter 293T cells containing a lox-STOP-lox-GFP cassette were cultured in Iscove's medium (Invitrogen Life Technologies) containing 10% FBS, 100 IU/ml penicillin, and 100 µg/ml streptomycin. Transductions were performed by adding diluted viral supernatant to the cells in the presence of 8 µg/mL polybrene (Sigma). Cells were transduced for 24h, after which medium was refreshed. Harvesting of cells for flow cytometry was performed 5 days after transduction.

Flow cytometry

Cells were collected 5 days after transduction, washed in PBS, fixed in Fixation Buffer (BD Biosciences) and permeabilized with Perm Buffer III (BD Biosciences). They were then stained using the primary rabbit antibody anti-Myc (1:1000, Abcam ab32072) or anti-Mcl1 (1:1000, Cell Signaling 94296S) for 30 minutes at 4 degrees, washed in PBS and incubated for 15 minutes with an AlexaFluor647-conjugated secondary anti-rabbit

antibody (1:1000, Thermofisher). Stained cells were analyzed using a Becton Dickinson LSR FORTESSA. GFP and AlexaFluor647 expression of viable cells was measured using a 488 nm and 640 nm laser for excitation, respectively. Data analysis was performed using FlowJo software version 7.6.5.

PCRs and TIDE analyses

Amplification of *Rb1* exon 2 and *Pten* exon 7 was performed with specific primers spanning the target sites (FW_Rb1: TCACCATGCTAGCAGCTCTTC; RV_Rb1: AGCCAGTTCAATGGTTGTGGG; FW_Pten: TGTATTTAACCACACAGATCCTCA; RV_Pten: AACAAACTAAGGGTCGGGGC) and 1 µg DNA template using the Q5 high-fidelity PCR kit from NEB. Amplicons were run on 1% agarose gel and gel-purified using the Isolate II PCR and Gel kit (Bioline). PCR products were Sanger-sequenced using the FW primer and CRISPR/Cas9-induced editing efficacy was predicted and quantified as described (Brinkman *et al.*, 2014; http://tide.nki.nl). Untransduced cells were taken along as a control in each gRNA amplification.

Immunoblotting

Protein lysates were made using lysis buffer (20 mM Tris pH 8.0, 300 mM NaCl, 2% NP40, 20% glycerol, 10 mM EDTA) complemented with protease inhibitors (Roche) and quantified using the BCA Protein Assay Kit (Pierce). Protein lysates were loaded onto a 3-8% Tris-Acetate gradient Gel (Invitrogen) and transferred overnight onto PVDF membrane (Millipore, methanol pre-wetted) in transfer buffer (38 mM glycine, 5 mM TRIS and 0.01% SDS in PBS-T (0.5% Tween-20). Membranes were blocked in 5% ELK in TBS-T after which they were stained for four hours at room temperature using the primary antibody anti-Met (1:1000, Cell Signaling 4560S) or anti-phosphoMet (1:1000, Cell Signaling 3077S). Membranes were washed three times with 1% milk in PBS-T and incubated for 1 hr with an HRP-conjugated secondary antibody (1:2000, DAKO). Stained membranes were washed three times in 1% milk in PBS-T and developed using SuperSignal ECL (Pierce).

Organoids culture

WB1P and WB1P-Myc mammary tumor organoids were isolated and cultured as described (Duarte *et al.*, 2017). For cell viability assays, organoids were seeded (100,000 cells per well) in 40 µl complete mouse media/BME mixture on 24-well suspension plates and cultured for 5 days in the presence of S63845 (ApEXBiO). Cell viability was assessed using the resazurin-based Cell Titer Blue assay following manufacturer's protocol (Promega). Cell viability experiments were performed 3 times in triplicate and

data were analyzed with GraphPad Prism statistical software using nonlinear regression and extra sum-of-squares F-test. For the focused shRNA library screen in WB1P-Myc organoids (Duarte *et al.*, 2017), a small library of shRNA targeting candidate genes was built from the Mission shRNA collection (mouse TRC v1.0 collection) by pooling shRNAs targeting candidate genes (*Mcl1*, *Gabpb2*, *Arnt*, *Setdb1*, *Tars*, *Golph3l*, *Lass2* and *Mllt11*) and control genes (*Plk1*, *Nlrp5*, *Crygb* and *Taar8a*). Organoids were transduced at MOI 0.3 and analyzed for shRNA representation at day 0, 7 and 14. MAGeCK software was used to compute RRA scores for all genes to identify relative shRNA depletion.

Meta-analysis of four human breast cancer datasets

Curated copy-number and mutation data for the METABRIC, TCGA and MSK-impact datasets were downloaded from cBioPortal (http://cbioportal.org, 13/10/2017), after which the downloaded mutation data was filtered for deleterious mutations (Missense_Mutation, Nonsense_mutation, Frame_Shift_Del and Frame_Shift_Ins). Similarly, copy-number data were filtered for high-level amplifications (amp) or homozygous deletions (homdel). Besides this, the MSK-impact dataset was filtered to include only breast cancers. Mutation and copy-number data for the BASIS dataset were obtained from Supplementary Tables 4, 14 and 20 accompanying reference (Nik-Zainal *et al.*, 2016) and filtered using similar criteria as the other datasets. The resulting datasets were merged and, where possible, annotated with the ER, PR and HER2 status of the corresponding samples. To select for samples with deleterious missense mutations in *BRCA1*, *BRCA1* missense mutations were annotated for their expected pathogenicity using the Breast Cancer Information Core (BIC) database (http://research.nhgri.nih.gov/bic) and Align-GVGD (http://agvgd.iarc.fr). We only selected samples with *BRCA1* missense mutations that were considered to be pathogenic (annotated as clinically important by BIC or Align-GVGD assigned class C15, C25 and C65). The final dataset was visualized using a custom script, focusing on cancer-associated genes, as defined by cBioPortal (http://cbioportal.org).

RNA Sequencing

llumina TruSeq mRNA libraries were generated and sequenced with 50-65 base single reads on a HiSeq 2500 using V4 chemistry (Illumina Inc., San Diego) as previously described (Henneman *et al.*, 2015). The resulting reads were trimmed using Cutadapt (version 1.15) to remove any remaining adapter sequences and to filter reads shorter than 20 bp after trimming to ensure good mappability. The trimmed reads were aligned to the GRCm38 reference genome using STAR (version 2.5.3a). QC statistics from Fastqc (version 0.11.5) and the above-mentioned tools were collected and summarized using Multiqc (version 1.1). Gene expression counts were generated by featureCounts (version 1.5.2) using gene definitions from Ensembl GRCm38 version 89. Normalized

expression values were obtained by correcting for differences in sequencing depth between samples using DESeqs median-of-ratios approach and then log-transforming the normalized counts. The entire analysis was implemented using Snakemake and is freely available on GitHub (https://github.com/jrderuiter/snakemake-rnaseq).

Generation of CNA profiles and data analysis

llumina HiSeq 2500 using V4 chemistry (Illumina Inc., San Diego) was performed as previously described (Henneman *et al.*, 2015). The resulting reads were trimmed using Cutadapt (version 1.15) to remove any remaining adapter sequences and trim reads longer to a length of 50bp for QDNAseq. Additionally, reads shorter than 20 bp after trimming were removed to ensure good mappability. The trimmed reads were aligned to the the GRCm38 reference genome using BWA aln (version 0.7.15). QC statistics from Fastqc (version 0.11.5) and the above-mentioned tools were collected and summarized using Multiqc (version 1.1). The resulting alignments were analyzed using QDNAseq (version 1.14.0) using the mm10 reference genome (with a 50K bin size, 50bp read lengths and default settings for other parameters) to generate copy-number logratios, segmented profiles and calls. The segmented profiles were analyzed using RUBIC (version 1.0.3; 6) to identify recurrent CNAs regions (focal threshold = 1e+08, min probes = 4 and FDR = 0.25). Genes with copy-number values were identified using a custom script, in which missing values were imputed from surrounding bins (with window size = 11, requiring at least 5 non-missing values). The entire analysis was implemented using Snakemake and is freely available on GitHub (https://github.com/jrderuiter/snakemake-cnvseq). Copy-number instability was scored by calculating the fraction of bins with logratio values above/below a threshold of +/-0.5 in the segmented copy-number data.

CNA analysis of BLBCs from TGCA

Segmented copy-number data for the TCGA breast cancer samples were downloaded from firebrowse (version 2016_01_28). These data were matched to subtype annotations from TCGA and filtered for BLBC samples. This BLBC dataset was analyzed using RUBIC (version 1.0.3) to identify recurrent CNAs (with focal threshold = 1e+07, min probes = 260000 and FDR = 0.25).

Comparative oncogenomics analysis

Candidate genes were initially selected by identifying mouse genes that were recurrently amplified/deleted in the RUBIC analysis of the combined germline/somatic Myc-driven mouse tumors. These candidates were subsequently annotated for their orthologous human genes using Ensembl Biomart (GRCH37) and filtered for candidates

whose orthologues were also recurrently aberrated in the RUBIC analysis of the human BLBCs. To filter for correlation with expression, we calculated the Spearman correlation between copy-number calls and gene expression values of the remaining candidate genes and selected genes with an absolute correlation > 0.2, resulting in a list of cross-species candidates.

Mouse studies

Myc murine cDNA was obtained from a cDNA clone (Clone 8861953, Source BioScience), sequence-verified and inserted as FseI-PmeI fragment into the *Frt-invCag-IRES-Luc* shuttle vector (Huijbers *et al.,* 2014), resulting in *Frt-invCag-Myc-IRES-Luc. Frt-invCag-Met-IRES-Luc* and *Frt-invCag-Cas9-IRES-Luc* were described in (Henneman *et al.*, 2015) and (Annunziato *et al.,* 2016). Flp-mediated knockin of the shuttle vectors in the *WapCre;Brca1*$^{F/F}$*;Trp53*$^{F/F}$*;Col1a1-frt* GEMM-ESC was performed as described (Huijbers *et al.,* 2014). Chimeric animals were crossed with WB1P or B1P mice to generate the experimental cohorts. *WapCre, Brca1*$^{F/F}$, *Trp53*$^{F/F}$ and knockin alleles were detected using PCR as described (Liu *et al.,* 2007; Huijbers *et al.,* 2014; Annunziato *et al.,* 2016). *In vivo* bioluminescence imaging was performed as described (Henneman *et al.,* 2015) by using a cooled CCD system (Xenogen Corp., CA, USA) coupled to Living Image acquisition and analysis software (Xenogen). Intraductal injections were performed as described (Krause *et al.,* 2013; Annunziato *et al.,* 2016). Lentiviral titers ranging from 2-20x10^8 TU/mL were used.

Orthotopic transplantation of WB1P and WB1P-Myc mammary tumors or organoids was performed by implanting small tumor fragments or cells into the fourth right mammary fat pad of nude mice as described previously (Duarte *et al.*, 2017). Treatment was initiated when tumors reached a size of ~100 mm^3 (formula for tumor volume: 0.5 × length × $width^2$). Cisplatin (6 mg/kg i.v.) was administered at day 0 and 14. Olaparib (100 mg/kg i.p.) and AZD2461 (100 mg/kg per os) were administered daily for 28 consecutive days. S63845 (25 mg/kg i.v.) was administered once-weekly for 5 weeks (Merino *et al.*, 2017). For experiments with PDX-110 (Merino *et al.*, 2017), thawed single cell suspensions of the tumor were transplanted orthotopically into the fourth right mammary fat pad of *NOD-SCID-IL2R*$\gamma_c^{-/-}$ mice. Treatment was initiated when tumors reached a size of ~100 mm^3. Olaparib (50 mg/kg i.p.) was administered 5 days out of 7 for 4 weeks. S63845 (25 mg/kg i.v.) was administered once-weekly for 4 weeks. Vehicle was DMSO/10% (2-hydroxypropyl-b-cyclodextrin) for olaparib and 20% (2-hydroxypropyl-b-cyclodextrin)/HCl for S63845.

Animal experiments were approved by the Animal Ethics Committees of the Netherlands Cancer Institute and the Walter and Eliza Hall Institute of Medical Research. Mice were bred and maintained in accordance with institutional, national and European guidelines for Animal Care and Use.

Histology and immunohistochemistry

Tissues were formalin-fixed overnight and paraffin-embedded by routine procedures. Haematoxylin and eosin staining was performed as described (Doornebal *et al.,* 2013). Immunohistochemical stainings were processed as described (Henneman *et al.,* 2015; Doornebal *et al.,* 2013). For MYC and MCL1 immunohistochemistry, primary rabbit antibody anti-Myc (1:1000, Abcam ab32072) or anti-Mcl1 (1:1000, Cell Signaling 94296S) were used. All slides were digitally processed using the Aperio ScanScope (Aperio, Vista, CA, USA) and captured using ImageScope software version 12.0.0 (Aperio).

Supplementary Figure Legends

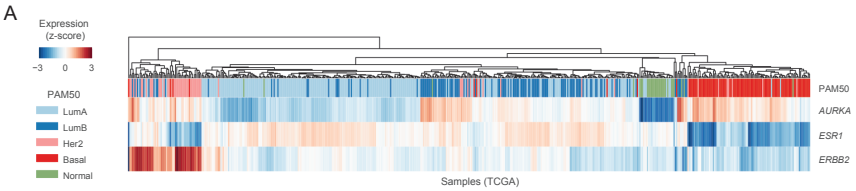

Supplementary Figure 1
Gene expression analysis of human breast cancer samples. (A) Unsupervised clustering (Euclidean distance, average linkage) of the human breast cancer samples from TCGA, using a three-genes signature that distinguishes the PAM50 subtypes (Haibe-Kains *et al.*, 2012). LumA, luminal A; LumB, luminal B.

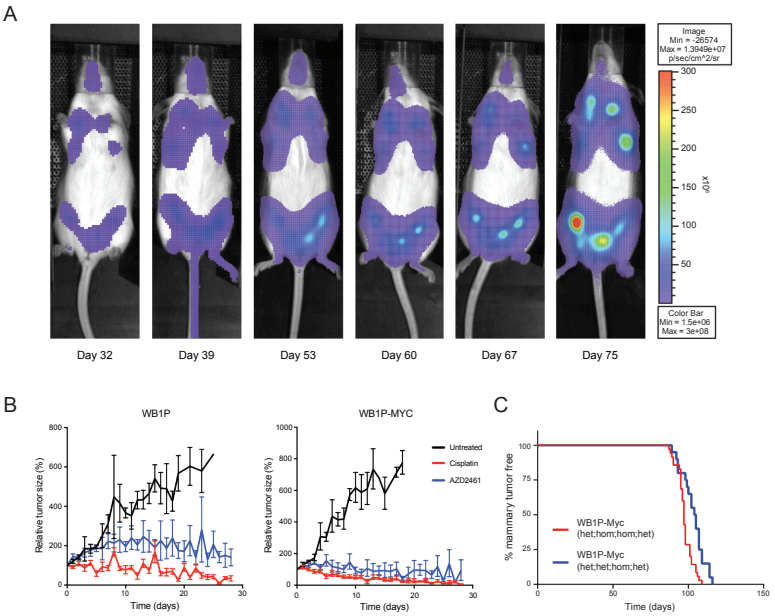

Supplementary Figure 2
Characterization of the WB1P-Myc mouse model. (A) Longitudinal *in vivo* bioluminescence imaging of luciferase expression in a WB1P-Myc female, showing signal build-up over time. (B) Response of WB1P and WB1P-Myc tumors to cisplatin and PARP inhibitors, as visualized by tumor volume curves. Small fragments of WB1P and WB1P-Myc tumors were transplanted in the fourth mammary fat pad of nude mice (n=36 per donor). When tumors had reached a size of 100 mm^3, mice were treated with 6 mg kg^{-1} cisplatin (administered i.v. on day 0 and day 14), 100 mg kg^{-1} AZD2461 (administered daily by per os, for 28 consecutive days) or vehicle. Error bars represent standard error of the mean. (C) Kaplan-Meier curves showing mammary tumor-specific survival for the different genotypes. *WapCre;Brca1*$^{F/F}$*;Trp53*$^{F/F}$*;Col1a1*$^{invCAG\text{-}Myc\text{-}IRES\text{-}Luc/+}$ (WB1P-Myc) females (n=35) showed a reduced mammary tumor-specific survival compared to *WapCre;Brca1*$^{F/+}$*;Trp53*$^{F/F}$*;Col1a1*$^{invCAG\text{-}Myc\text{-}IRES\text{-}Luc/+}$ (n=20) littermates (97 days vs 105 days; ***P < 0.001 by Mantel-Cox test).

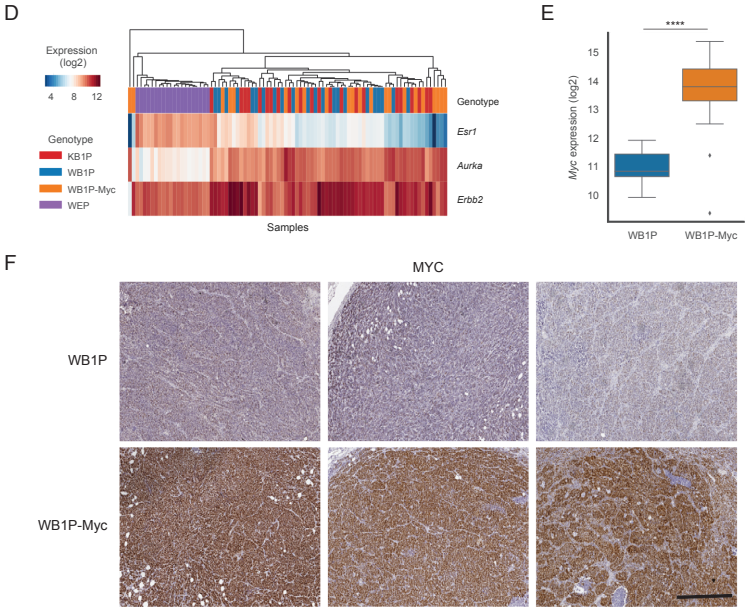

Supplementary Figure 2 Continued.
(D) Unsupervised clustering (Euclidean distance, average linkage) of WB1P and WB1P-Myc tumors with tumors derived from published mouse models of luminal (*WapCre;Cdh1*$^{F/F}$*;Pten*$^{F/F}$, WEP) and basal-like (*K14Cre;Brca1*$^{F/F}$*;Trp53*$^{F/F}$, KB1P) breast cancer, using a three-genes signature that distinguishes the PAM50 subtypes (Haibe-Kains *et al.*, 2012). (E) *Myc* expression levels in WB1P and WB1P-Myc tumors; ****$P < 0.0001$ (two-sided Mann-Whitney U test). Boxes extend from the third (Q3) to the first (Q1) quartile (interquartile range, IQR), with the line at the median; whiskers extend to Q3 + 1.5 × IQR and to Q1 − 1.5 × IQR. Points beyond the ends of the whiskers are outliers. (F) Immunohistochemical detection of MYC in multiple independent WB1P and WB1P-Myc tumors. Bar, 400 µM.

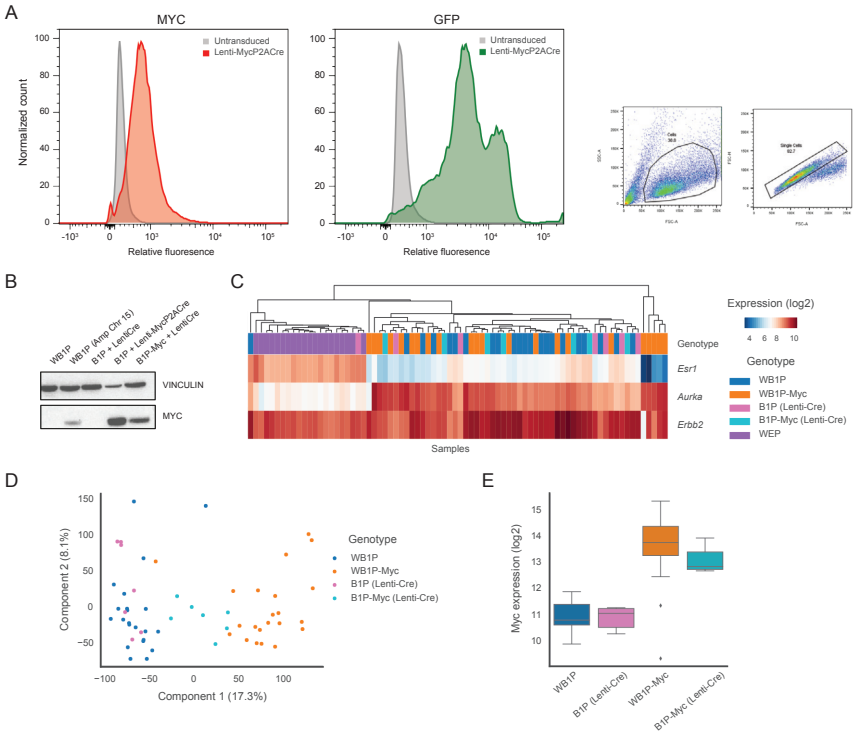

Supplementary Figure 3

Non-germline models with *Myc* overexpression. (A) *In vitro* validation of Lenti-MycP2ACre in Cre-reporter cells (containing a lox-STOP-lox-GFP cassette) 5 days after transduction. Expression of MYC as visualized by FACS using an anti-MYC antibody and FACS analysis of Cre-recombined GFP-positive cells are shown. A figure exemplifying the gating strategy is provided on the right. (B) Expression of MYC in independent tumors as visualized by immunoblotting using anti-MYC antibody. Sample order: WB1P tumor without chromosome 15 amplification; WB1P tumor with chromosome 15 amplification; tumor from B1P mouse injected with Lenti-Cre; tumor from B1P mouse injected with Lenti-MycP2ACre; tumor from B1P-Myc mouse injected with Lenti-Cre. (C) Unsupervised clustering (Euclidean distance, average linkage) of the tumors from germline and somatic models using the three-genes PAM50 signature (Haibe-Kains *et al.*, 2012), showing that tumors from the somatic models retain the basal expression profiles observed in tumors from the germline models. (D) PCA plot comparing WB1P and WB1P-Myc tumors to tumors from the non-germline models (Lenti-Cre injected B1P and B1P-Myc mice) using global gene expression profiles. (E) *Myc* expression levels in tumors from germline and non-germline models. Boxes extend from the third (Q3) to the first (Q1) quartile (interquartile range, IQR), with the line at the median; whiskers extend to Q3 + 1.5 × IQR and to Q1 − 1.5 × IQR. Points beyond the ends of the whiskers are outliers.

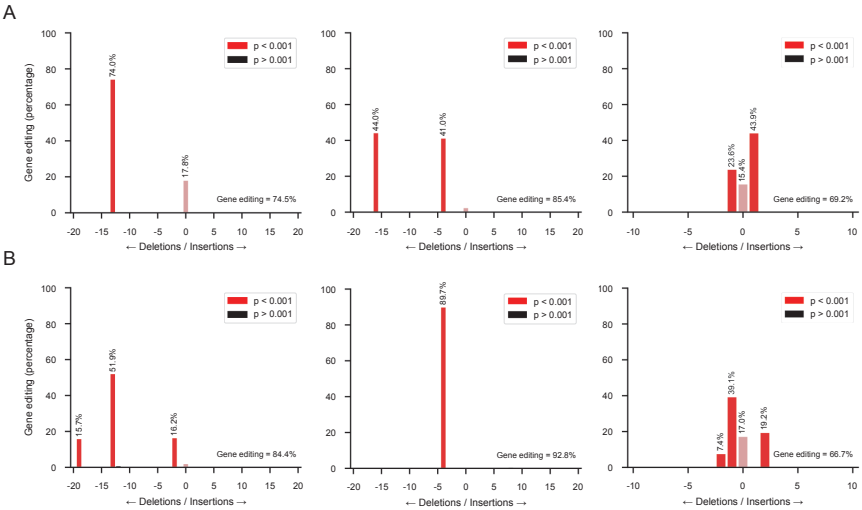

Supplementary Figure 4

CRISPR-mediated somatic gene disruption of *Rb1* and *Pten*. (A-B) TIDE analysis showing the spectrum of insertions/deletions (indels) of the targeted *Rb1* (A) and *Pten* (B) alleles in multiple independent tumors from WB1P-Cas9 mice injected with Lenti-sg*Rb1*-Myc and Lenti-sg*Pten*-Myc, respectively.

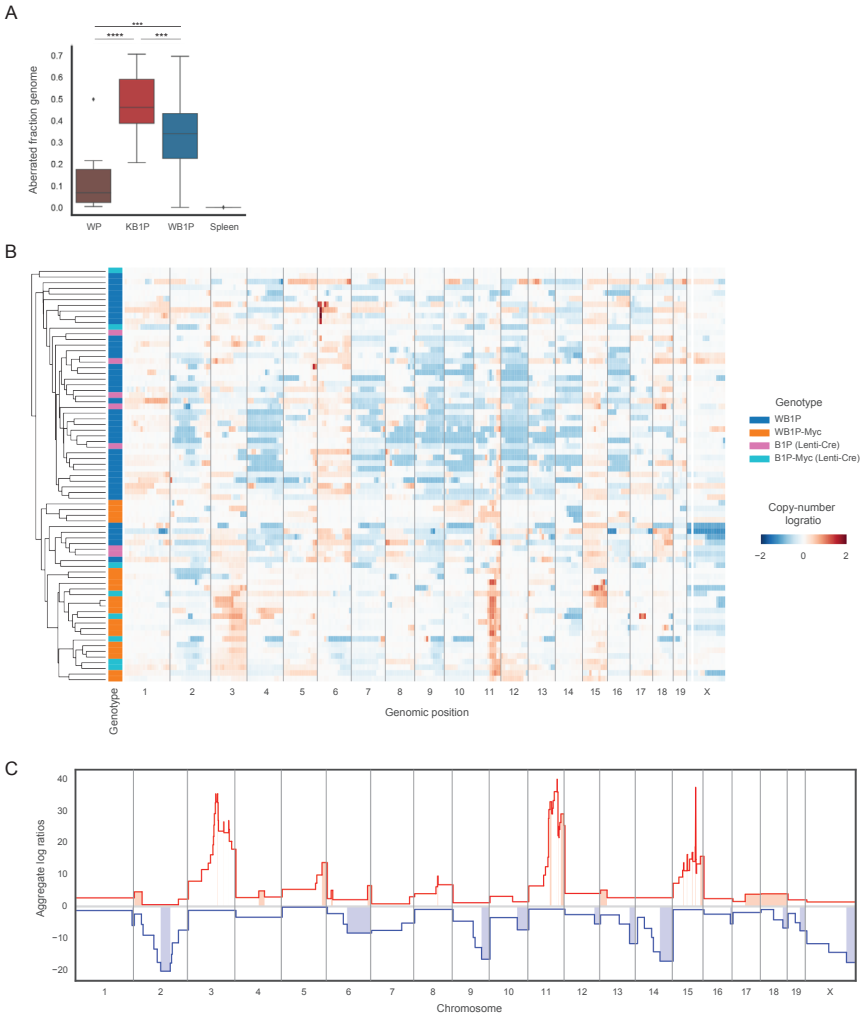

Supplementary Figure 5

Genomic instability of WB1P and WB1P-Myc tumors. (A) Genomic instability scores of WP, WB1P and KB1P tumors; ***$P < 0.001$ and ****$P < 0.0001$ (two-sided Mann-Whitney U test). Scores for spleen samples from WB1P mice are shown as reference. Boxes extend from the third (Q3) to the first (Q1) quartile (interquartile range, IQR), with the line at the median; whiskers extend to Q3 + 1.5 × IQR and to Q1 − 1.5 × IQR. Points beyond the ends of the whiskers are outliers. (B) Unsupervised clustering (correlation distance, average linkage) of the tumors from somatic and germline models based on their copy-number profiles. Tumors from the somatic models mainly cluster together with their germline counterparts, demonstrating that these tumors have similar patterns of copy-number aberrations. (C) Overview of the recurrently aberrated regions identified by RUBIC in the combined set of MYC-driven tumors from the germline and somatic models.

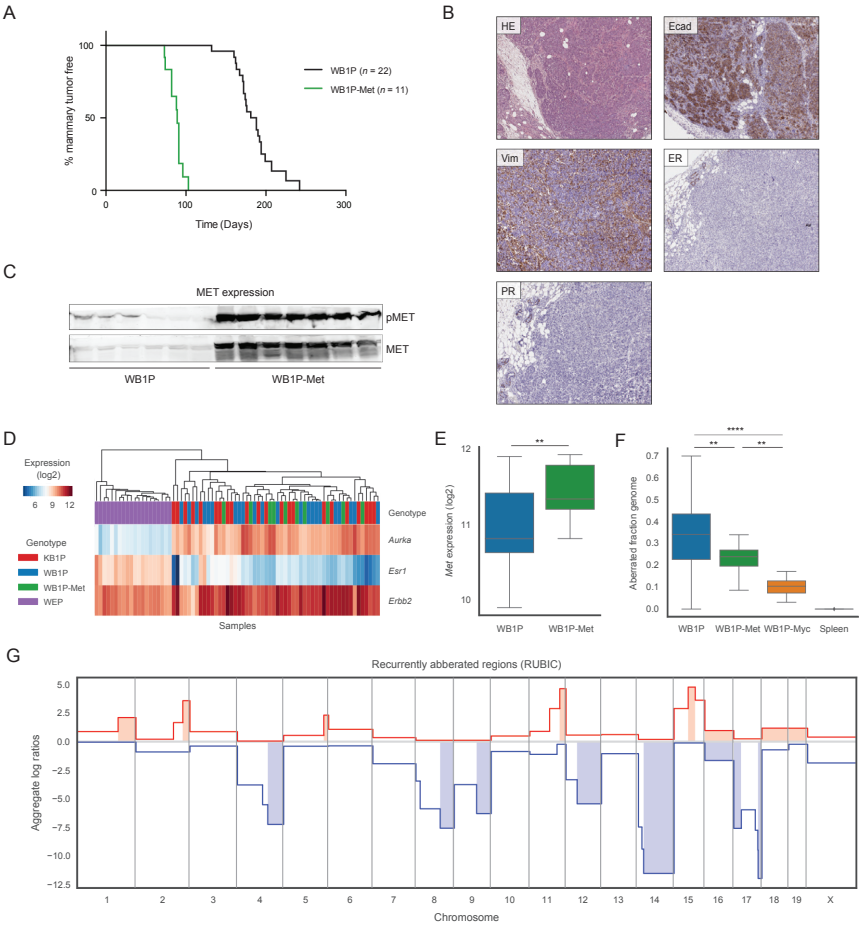

Supplementary Figure 6

Characterization of the WB1P-Met mouse model. (A) Kaplan-Meier curves showing mammary tumor-specific survival for the different genotypes. *WapCre;Brca1*$^{F/F}$*;Trp53*$^{F/F}$*;Col1a1*$^{invCAG\text{-}Met\text{-}IRES\text{-}Luc/+}$ (WB1P-Met) females showed a reduced mammary tumor-specific survival compared to WB1P littermates (89 days vs 188 days; ****$P < 0.0001$ by Mantel-Cox test). (B) Representative hematoxylin and eosin (HE) staining and immunohistochemical detection of E-cadherin, vimentin, ER and PR in WB1P-Met tumors. (C) Expression and activity of MET in independent tumors from WB1P and WB1P-Met mice, as visualized by immunoblotting using anti-MET and anti-phosphoMET antibodies. (D) Unsupervised clustering (Euclidean distance, average linkage) of WB1P and WB1P-Met tumors with tumors derived from published mouse models of luminal (*WapCre;Cdh1*$^{F/F}$*;Pten*$^{F/F}$, WEP) and basal-like (*K14Cre;Brca1*$^{F/F}$*;Trp53*$^{F/F}$, KB1P) breast cancer, using a three-genes signature that distinguishes the PAM50 subtypes (Haibe-Kains *et al.*, 2012). (E) *Met* expression levels in WB1P and WB1P-Met tumors; **$P < 0.01$ (two-sided Mann-Whitney U test). Boxes extend from the third (Q3) to the first (Q1) quartile (interquartile range, IQR), with the line at the median; whiskers extend to Q3 + 1.5 × IQR and to Q1 − 1.5 × IQR. (F) Genomic instability of WB1P, WB1P-Met and WB1P-Myc tumors; **$P < 0.01$ and ****$P < 0.0001$ (two-sided Mann-Whitney U test). Scores for spleen samples from WB1P mice are shown as reference. (G) Genome-wide RUBIC analysis of the CNV profiles of WB1P-Met tumors. Significant amplifications and deletions are marked by light red and blue columns, respectively.

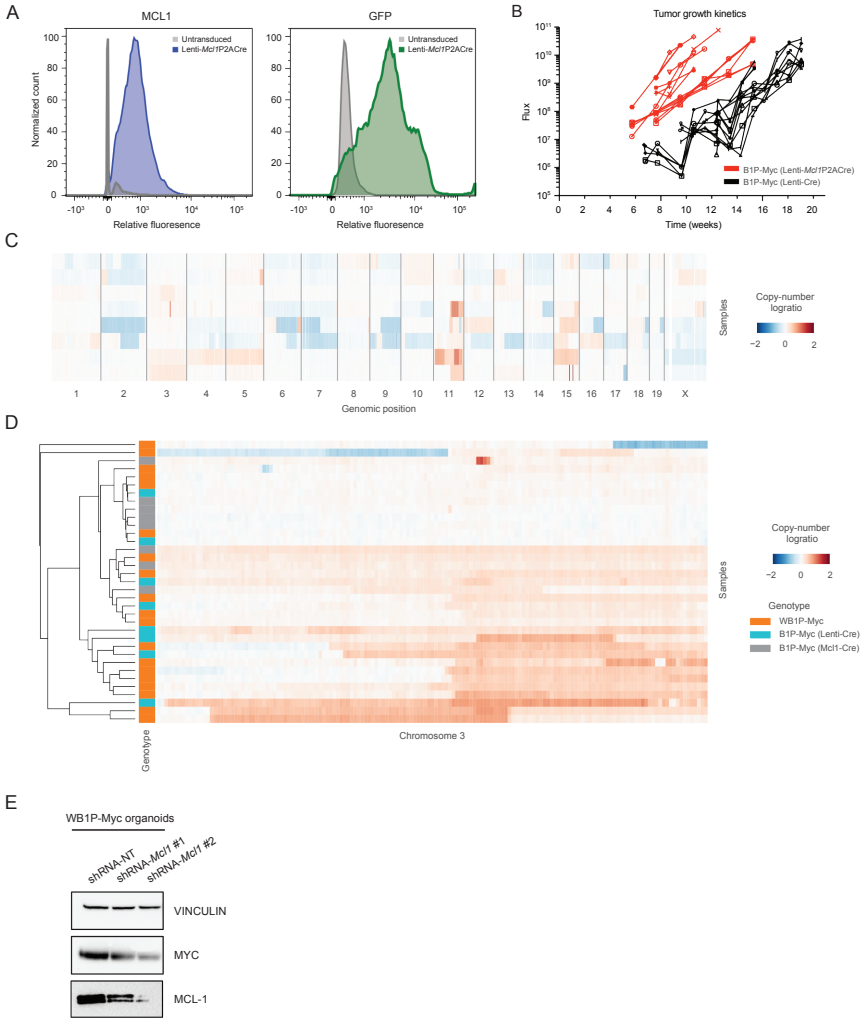

Supplementary Figure 7

Validation of MCL1 as a driver in BRCA1-associated TNBC. (A) *In vitro* validation of Lenti-Mcl1P2ACre in Cre-reporter cells 5 days after transduction. Expression of MCL1 as visualized by FACS using an anti-MCL1 antibody and FACS analysis of Cre-recombined GFP-positive cells are shown. (B) Longitudinal *in vivo* bioluminescence imaging of luciferase expression in B1P-Myc animals injected with Lenti-Cre (black lines) or Lenti-Mcl1P2ACre (red lines), showing signal build-up over time. (C) Heatmap showing the copy-number logratios for tumors from B1P-Myc females injected with Lenti-Mcl1P2ACre, showing that recurrent gains on chromosomes 11 and 15 are retained, whilst the gain on chromosome 3 is less pronounced. (D) Unsupervised clustering (Euclidean distance, average linkage) of MYC-driven tumors from germline and somatic models (WB1P-Myc tumors and tumors from Lenti-Cre injected B1P-Myc mice) together with tumors from B1P-Myc females injected with Lenti-Mcl1P2ACre. The clustering shows that the focal gain surrounding *Mcl1* is lost in the majority of tumors from Lenti-Mcl1P2ACre injected B1P-Myc females. (E) Expression of MYC and MCL1 in WB1P-Myc organoids transduced with a non-targeting shRNA or with two independent sh*Mcl1* vectors, as visualized by immunoblotting using anti-MYC antibody 5 days after transduction.

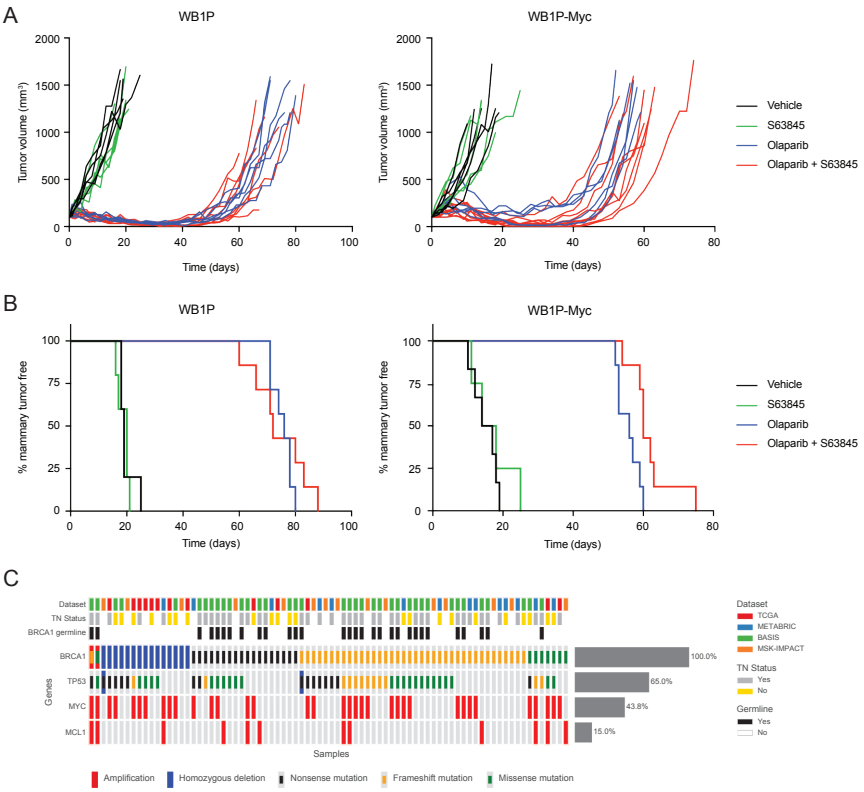

Supplementary Figure 8
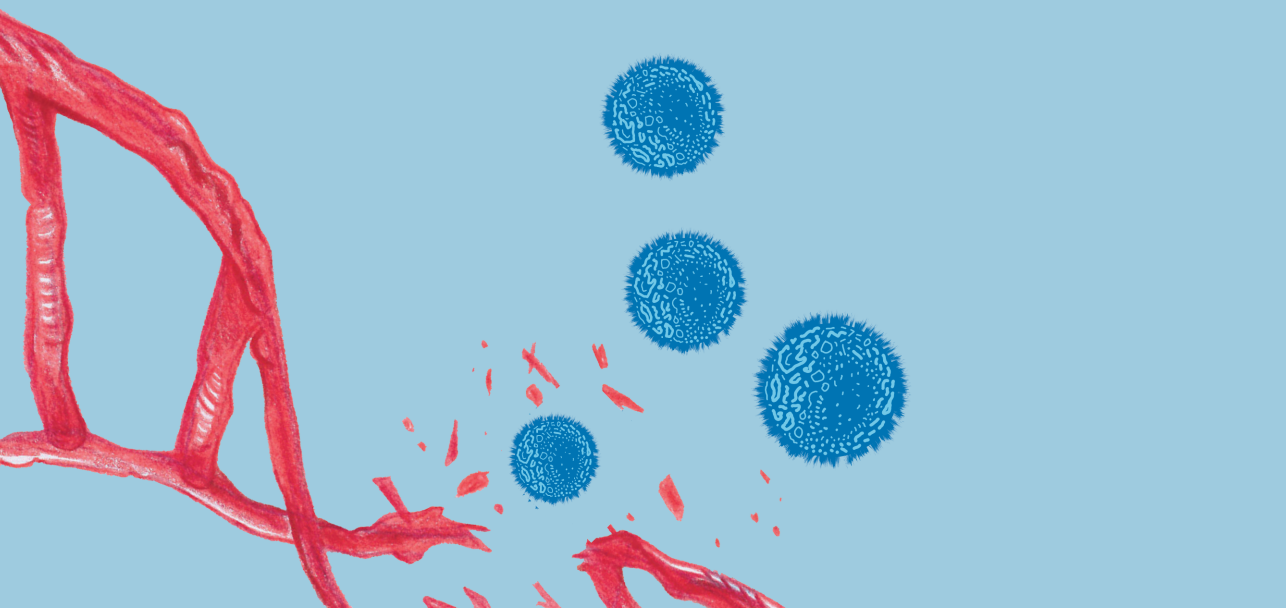
Treatment of WB1P and WB1P-Myc tumors with MCL1 and PARP inhibitors. (A-B) Response of organoid-derived WB1P and WB1P-Myc tumors to MCL1 and PARP inhibitors, as visualized by tumor volume curves (A) and Kaplan Meier curves (B). WB1P and WB1P-Myc organoid lines were transplanted in the fourth mammary fat pad of nude mice (n=24 per donor). When tumors had reached a size of 100 mm^3, mice were treated with 25 mg kg^{-1} S63845 (administered i.v. once weekly for 5 weeks), 100 mg kg^{-1} olaparib (administered i.p. daily for 28 consecutive days), both drugs or vehicle. S63845 shows minimal additive efficacy over olaparib alone in WB1P-Myc tumors (*$P < 0.05$ by Mantel-Cox test). (C) Overview of the mutations and copy-number events in our panel of 80 *BRCA1*-mutated human breast tumor samples for *TP53*, *MYC* and *MCL1*.